united nations
educational, scientific
and cultural
organization

international atomic
energy agency

the
abdus salam
international centre for theoretical physics

ICTP 40th Anniversary

SCHOOL ON SYNCHROTRON RADIATION AND APPLICATIONS
In memory of J.C. Fuggle & L. Fonda

19 April - 21 May 2004

Miramare - Trieste, Italy

1561/26

Glasses and glass-ceramics by WAXS

A. Benedetti

School on Synchrotron Radiation

Trieste - 7-13 May 2004

Glasses and glass-ceramics by WAXS

Alvise BENEDETTI

Dipartimento di CHIMICA FISICA

UNIVERSITA' CA' FOSCARI di VENEZIA

In contrast to conventional radiation source, the main properties of synchrotron radiation are

1) the extremely good instrumental resolution over extended angular ranges (for example, full widths at half maximum of <0.01° out to a d-spacing of 1Å at a wavelength of 0.7Å),

2) excellent peak-to-background discrimination,

3) peak shapes which are very well described by the commonly-used pseudo-Voigt function (including a simple and reliable asymmetry correction for axial divergence at lower angles),

4) high brigthness (large amount of flux in a well collimated beam)

5) an intense continuous wavelength distribution spectrum, from which monochromatized X-radiation can be selected and the consequent possibility of using anomalous scattering as a general probe of cation distribution for elements with Z>35.

Although there is no sharp dividing line between crystalline and so called amorphous materials, for clarity in this discussion we somewhat arbitrarily designate as *crystalline* those materials characterized by three-dimensional periodicity over appreciable distances, say, of the order of six or more unit translations. Conversely, materials possessing only one or two-dimensional, or lesser, degrees of order are referred to as *amorphous*.

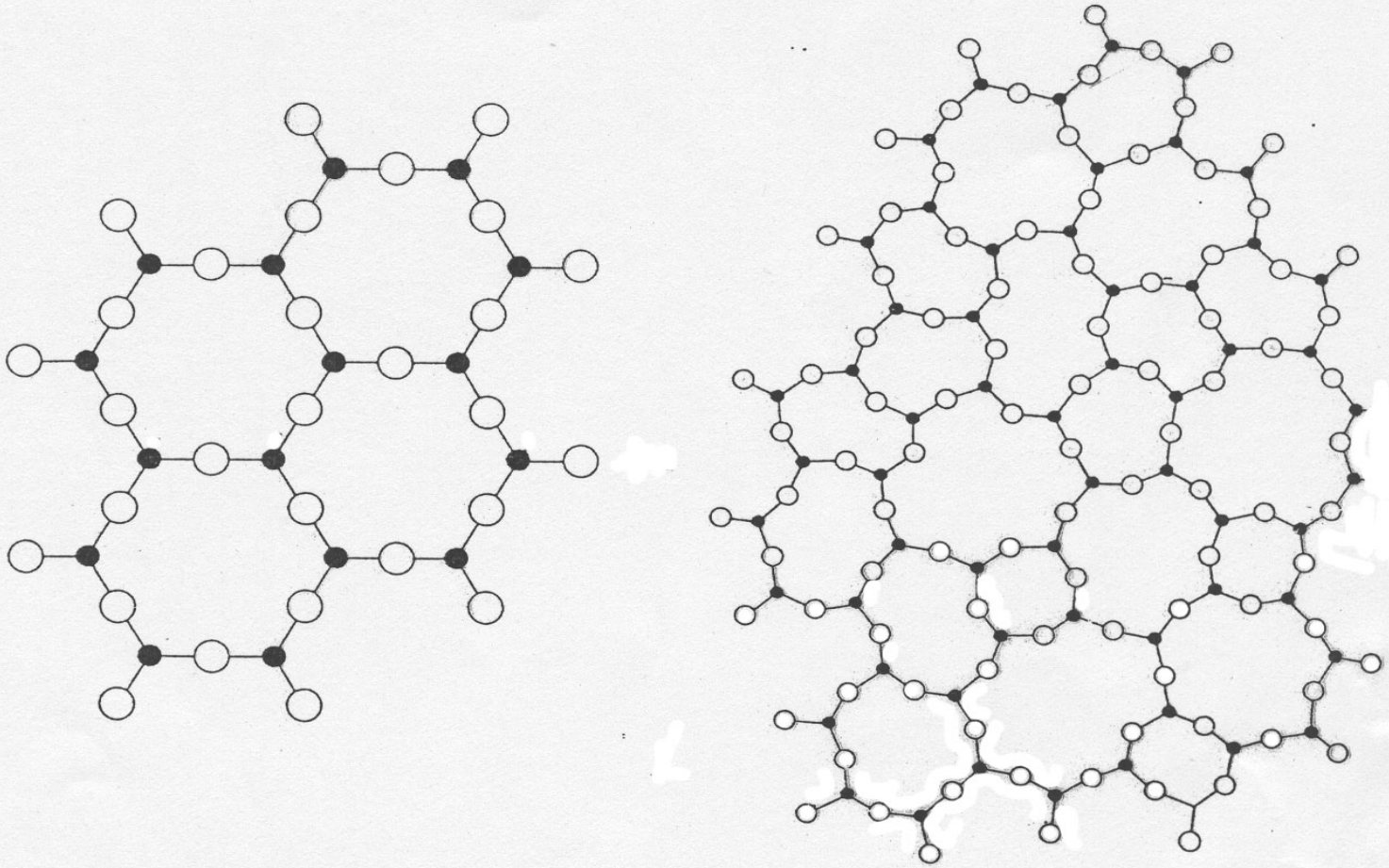

(A) (B)

Fig. 12-1. Two-dimensional representation of the difference between a crystal *A* and glass *B* of the same chemical composition A_2O_3. (From W. H. Zachariasen, *J. Am. Chem Soc.*, **54**, 3841 (1932), copyright by the American Chemical Society. Reprinted by permission of the copyright owner.)

For very small cluster containing few atoms it is preferable to calculate the pattern from the Debye formula.

If we consider a liquid, it has no structure with respect to a fixed origin since the atoms are continually moving about.

In an amorphous solid (glasses, glassy metals, resins, unoriented solid polymers), the atoms have permanent neighbours but there is no repeating structure, only local configurations.

Pd cubottaedric cluster :
11 shells; 5083 atoms
average diameter 50.6 Å
λ=1.54 Å

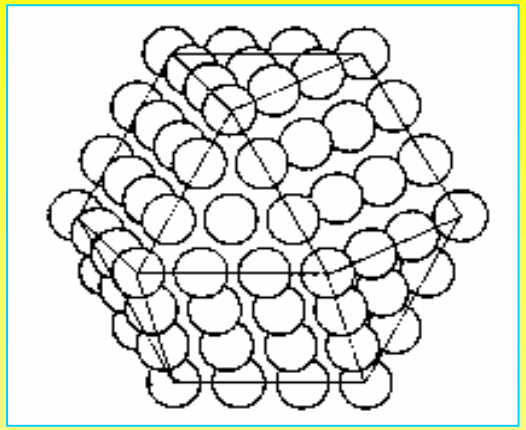

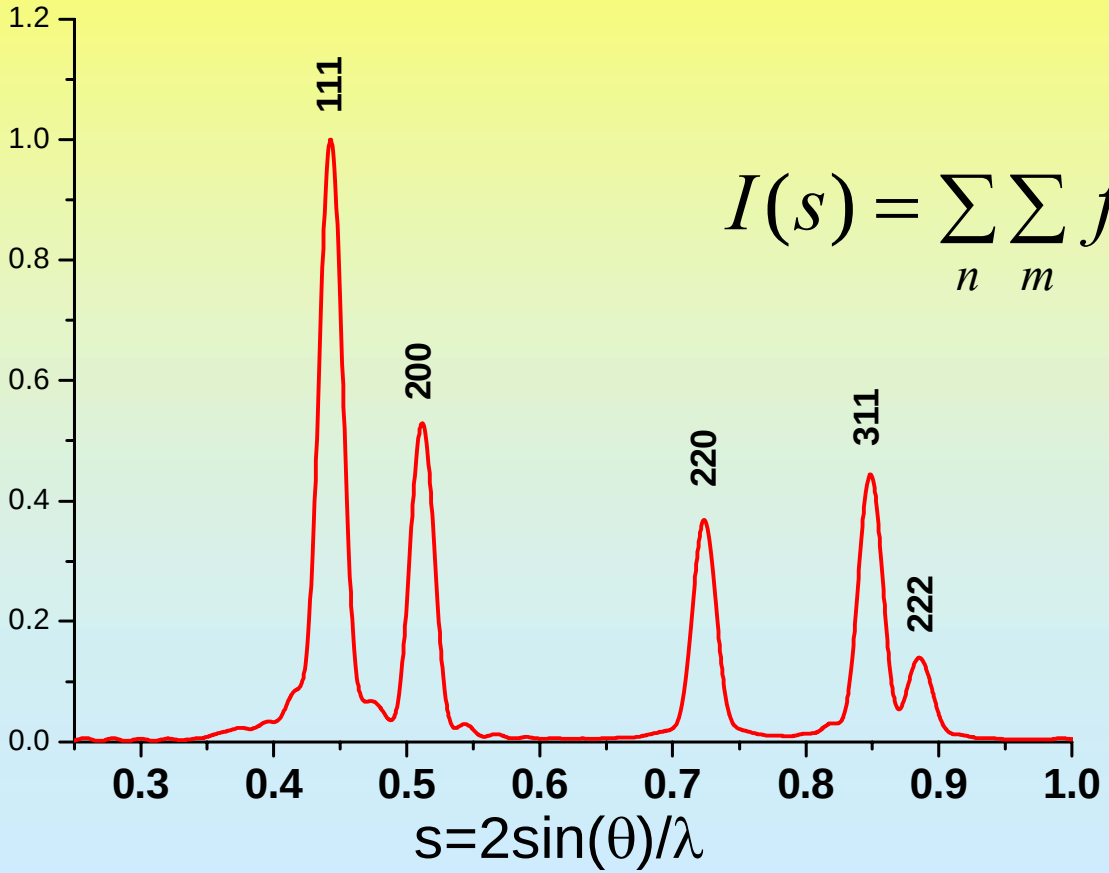

$$I(s) = \sum_n \sum_m f_n f_m \frac{\sin(2\pi\, s\, r_{nm})}{2\pi\, s\, r_{nm}}$$

The diffraction pattern from a amorphous sample (i.e. a glass) exhibits broad features, indicating the lack of translational symmetry in its structure.

The quantity obtained from a conventional scattering experiment is the ***radial distribution function*** (RDF), which is a description of the average environment of an atom, for example, in a glass.

$$I = Nf^2\left[1+\int_0^\infty 4\pi\rho(r)\frac{sin(hr)}{hr}dr\right]$$

Here $\rho(r)$ is the number of atoms per unit volume at a distance r from the reference atom, and $4\pi r^2\rho(r)dr$, as reported above, is the number of atoms contained in a spherical shell of radius r and thickness dr.

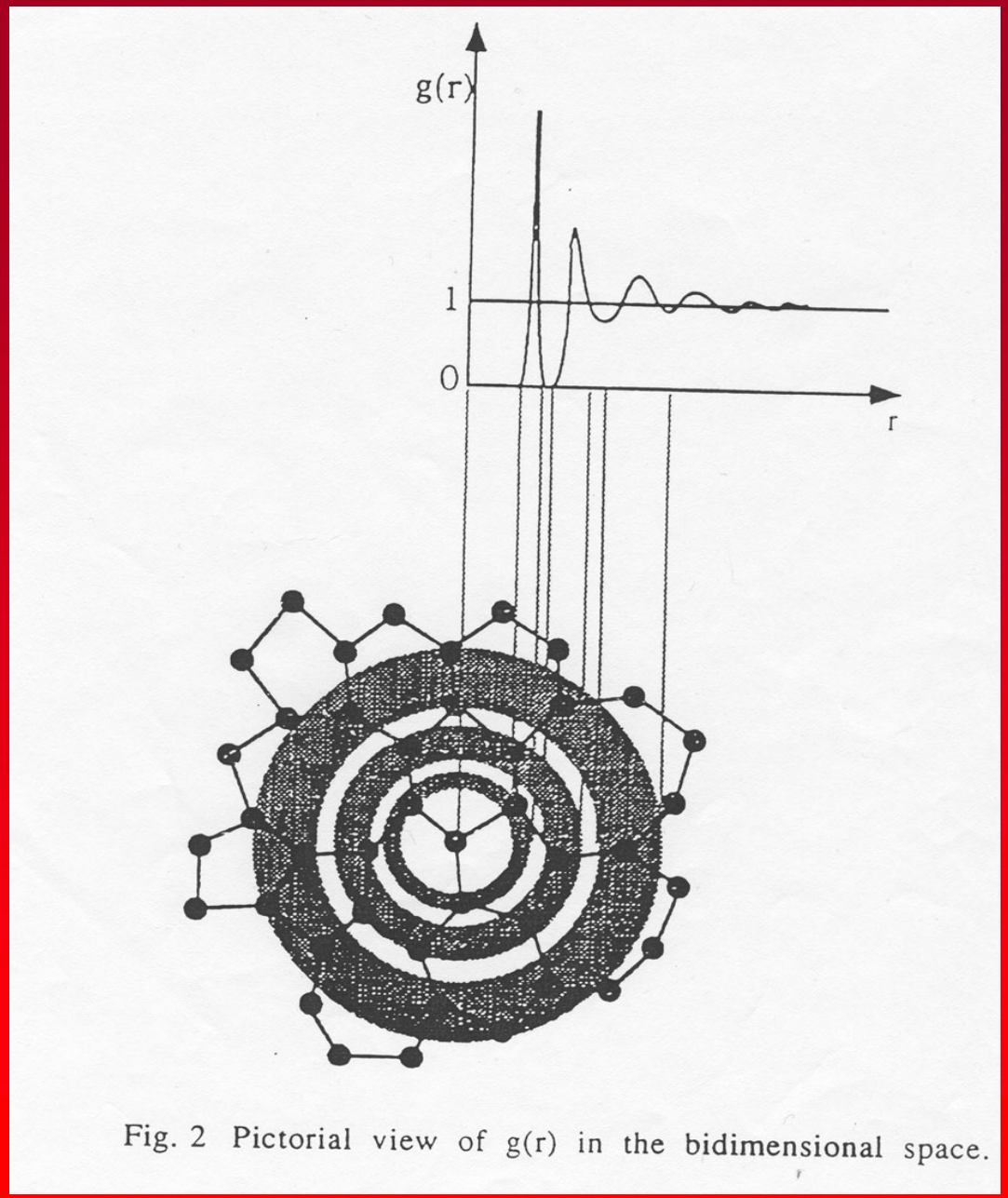

Fig. 2 Pictorial view of g(r) in the bidimensional space.

Letting ρ_0 be the average density of atoms in the sample, eq may be rewritten as

$$\frac{I}{Nf^2} - 1 = \int_0^\infty 4\pi r^2 [\rho(r) - \rho_0] \frac{sin(hr)}{hr} dr$$

By means of the Fourier integral theorem, this expression can be trasformed to

$$4\pi r^2 \rho(r) = 4\pi r^2 \rho_0 + \frac{2r}{\pi} \int_0^\infty hi(h) sin(hr) dh$$

The RDF is defined as $4\pi r^2\rho(r)$, where $\rho(r)$ is the radial density function and r is the radius; $\rho(r)$ is the average number density of atoms at a distance r from an average atom at the origin.

The RDF, therefore, is the number of atoms in a shell of unit thickness at a distance r.

The number of neighbors coordinating a central atom is obtained by integrating a peak in the RDF, and the average distance of these neighbors is obtained from the peak position.

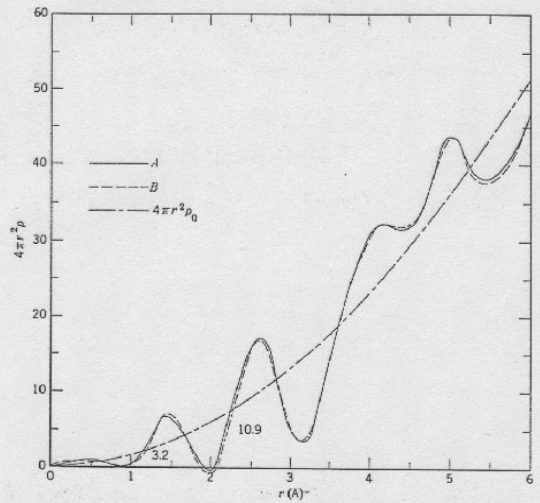

Fig. 12-11. RDF of carbon black as modified by (*A*) eliminating that portion of the *Si*(*S*) curve above $S = 8.4$ and (*B*) replacing it with the broken-line curve of Fig. 12-9.

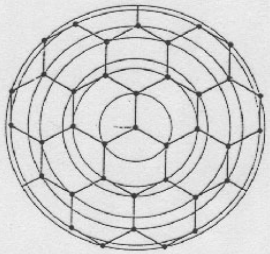

Fig. 12-22. Arrangement of carbon atom neighbors about a reference atom in a single [illegible]. [Courtesy of B. E. Warren, *J. Chem. Phys.*, **2**, 551 (1934).]

Table 12-4. Numbers of Neighbors and Distances in a Single Layer of the Graphite Structure

Number of Neighbors	Distance (Å)	Average Distance (Å)
3	1.42	1.42
6	2.46	2.60
3	2.84	
6	3.75	4.00
6	4.25	
6	4.92	5.00
6	5.11	

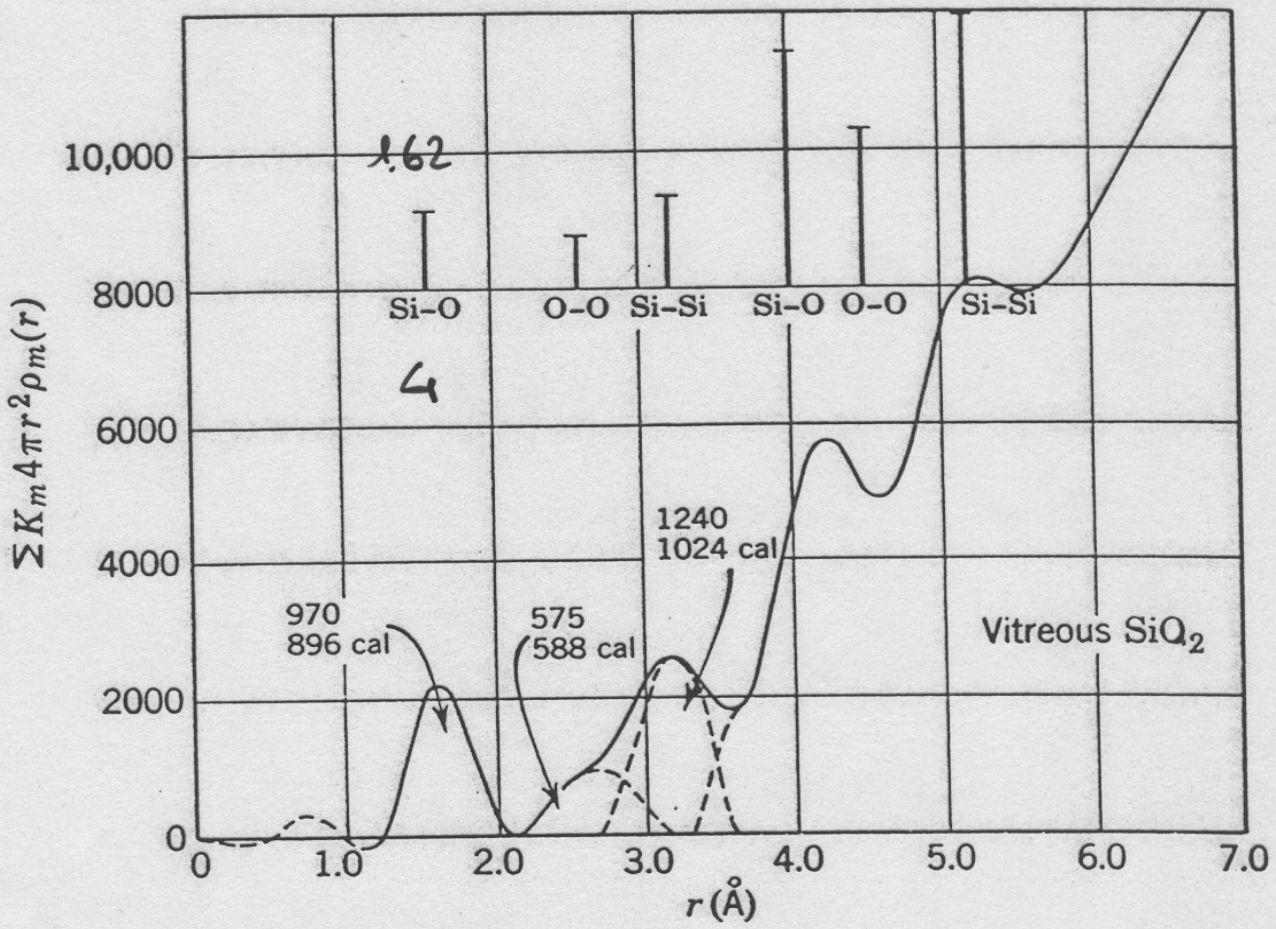

Fig. 12-25. Radial-distribution curve for vitreous SiO_2. [Courtesy of B. E. Warren, Krutter, and O. Morningstar, *J. Am. Ceram. Soc.*, **19**, 202 (1936).]

Even in one-component system, the interpretation of the RDF is difficult because the local structure is spherically averaged.

In a multicomponent system, the problem is even more complex because the average environment portrayed by the RDF might bear little resemblance to the actual environment of any given component.

Anomalous scattering experiments permit species-specific distribution functions to be obtained, which give a more direct view of the amorphous structure.

When the X-ray energy is close to an absorption edge of an atom, the X-ray scattering factor changes significantly through the ***anomalous scattering factors*** (ASF's) f' and f''. For example, the scattering factor of Se is reduced from its maximum value by approximately 10 electrons at the K absorption edge energy.

Therefore, Se (atomic number Z=34) scatters more like Cr (Z=24). Suppose scattering patterns are obtained from an Ag-Ge-Se glass at two X-ray energies close to the Se K absorption edge.

The scattering behaviour of Se is different at each energy, but the behaviour of Ge and Ag is the same. The difference between the two patterns can be related to the distance correlations involving Se atoms.

Anomalous Small-Angle X-ray Scattering

$$f = f_0 + f'(E) + f''(E)$$

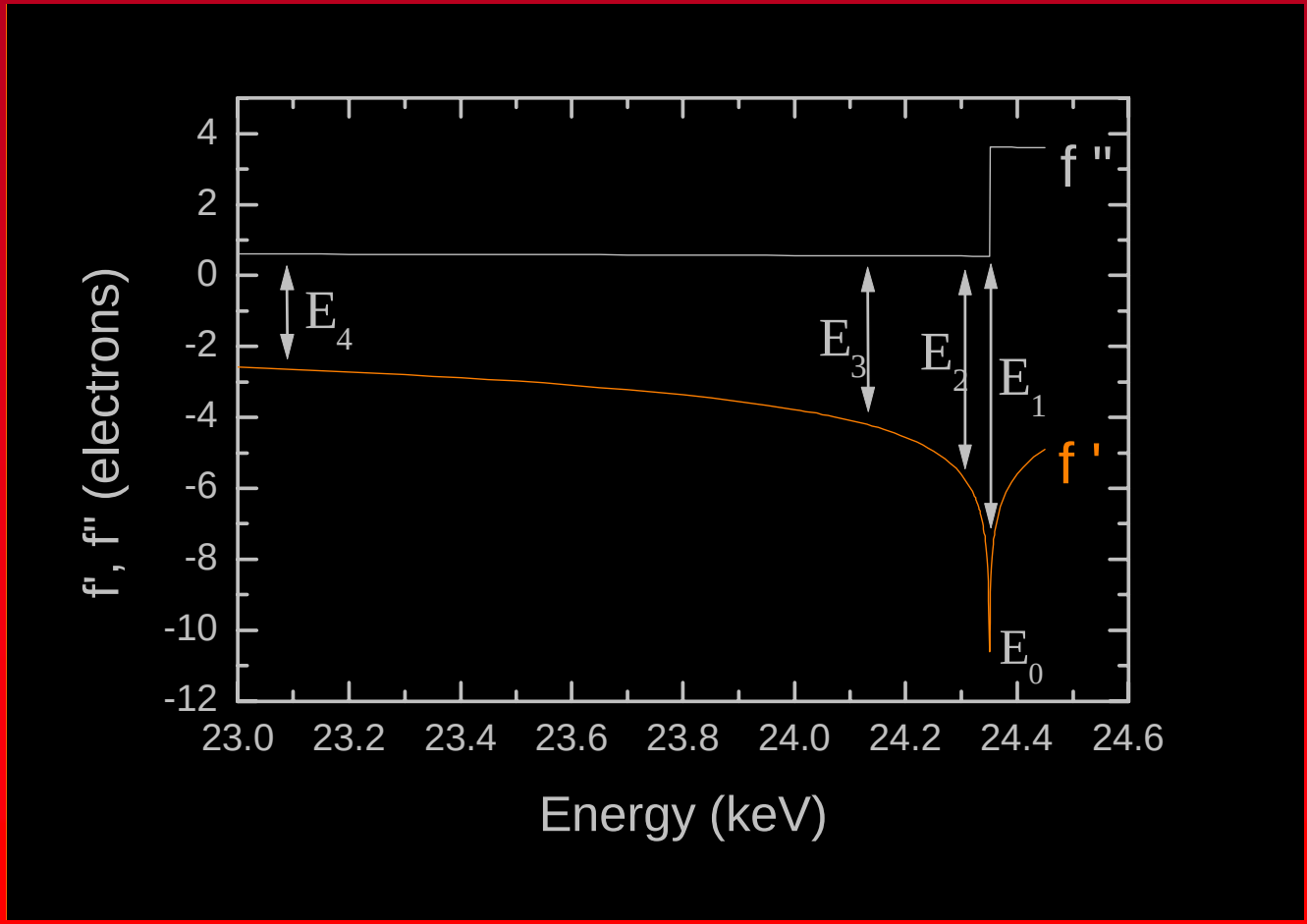

The Debye formula for the intensity is

$$I = \sum_m \sum_n f_m f_n \frac{\sin(hr_{mn})}{hr_{mn}}$$

The result of this type of experiment is the ***difference distribution function*** (DDF) around Se. The DDF is $4\pi r^2 \rho_{Se}(r)$, where $\rho_{Se}(r)$ is the density of atoms at a distance r from a central Se atom.

The idea of obtaining structural information from the derivative of the scattered X-ray intensity with respect to energy was first proposed by Shevchik.

However, the ***differential anomalous scattering*** (DAS) technique outlined above was first developed and applied experimentally to amorphous GeSe and glassy $GeSe_2$ by Fuoss.

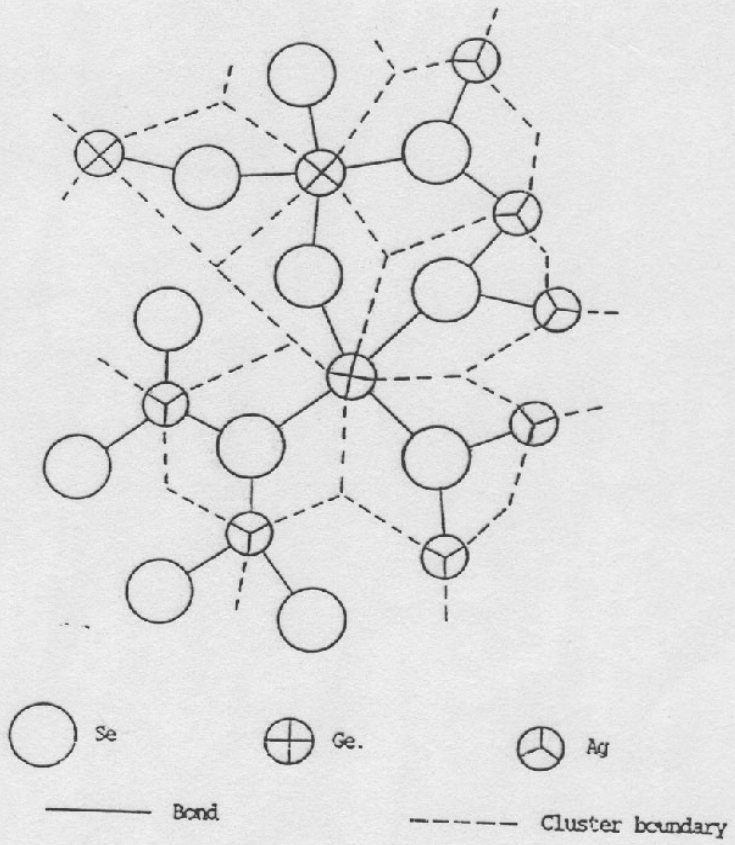

Figure 58: Schematic Illustration of Clusters in a Two-Dimensional Ag-Ge-Se Glass Structure. Each Se atom in the structure defines a cluster. Clusters share Ge and Ag atoms, which, for the purpose of illustration only, are assumed to have four and three Se near neighbors, respectively.

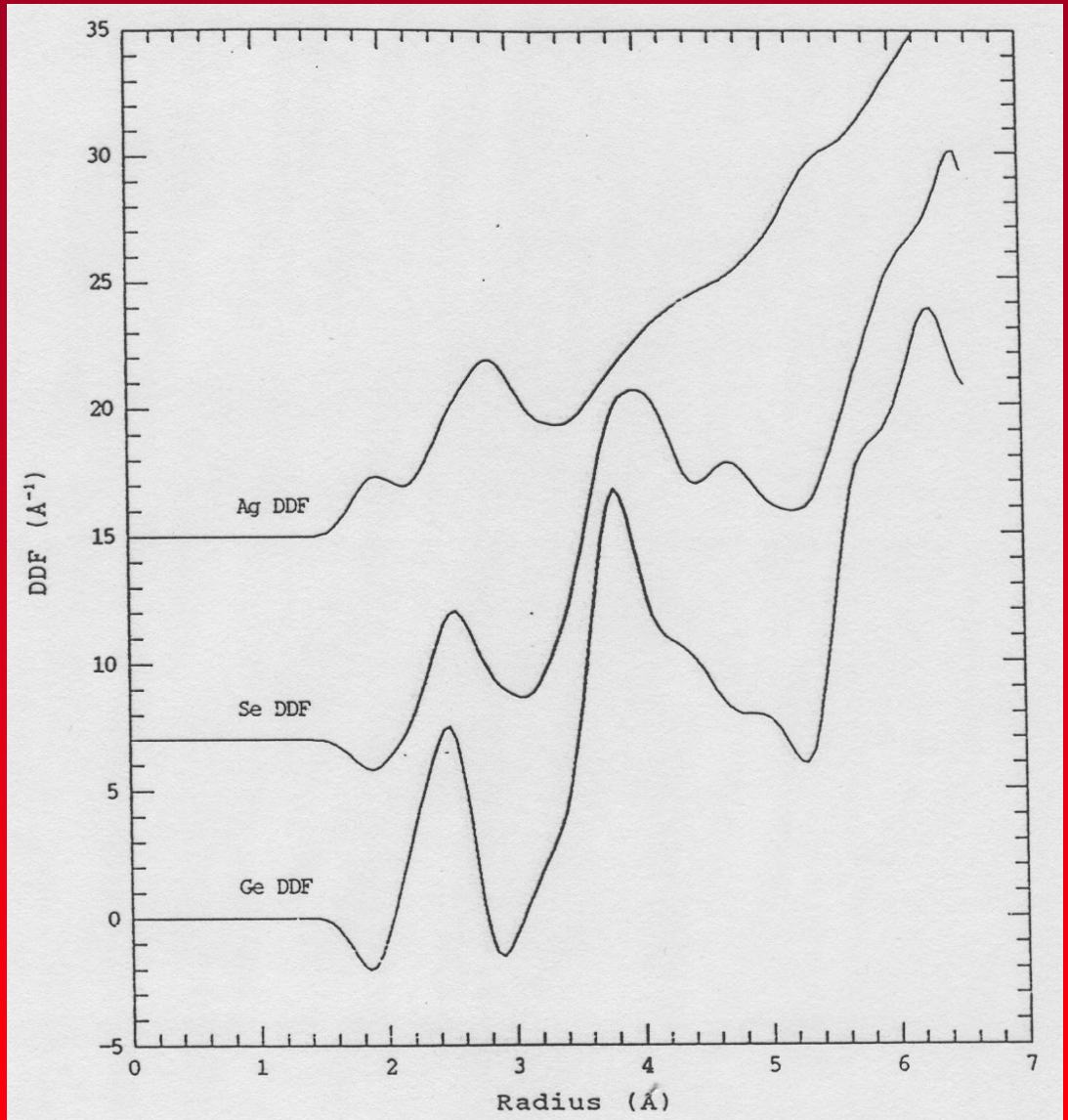

Figure 75: MEM DDF's. The scans at 11000, 11099, 12554, 12658, 25300, and 25500 eV have been used as input data. The vertical scale is shifted for each function.

The potential of anomalous scattering experiments is not limited to obtaining DDF's. It is possible to obtain the partial distribution function (PDF), in which the intensities of both the central atom and its neighbors are known. The $\alpha\beta$ PDF describes the distribution of β atoms around a central a atom; it is equal to $4\pi r^2\rho_{ab}(r)$, where $\rho_{ab}(r)$ is the number density of β atoms at α distance r from an a atom at the origin.

The total number α–β distances in the structure is constant, leading to the condition

$$X_a\rho_{ab}(r)=X_b\rho_{ba}(r)$$

where X is the mole fraction.

Keating demonstrated how M(M+1)/2 independent scattering experiments can be used to determine the same number of indipendent PDF's. In each experiment, the scattering factors of one or more of the components must be altered in indipendent way.

The energy dependence of the anomalous scattering factors provides one means to accomplish this.

If we consider a three components glass, six scattering patterns must be collected, two in the vicinity of the K absorption edge of each component.

The PDF's are difficult to obtain because the independence that can be achieved by varying the anomalous scattering factors is limited. In practice, the results are very sensitive to experimental error.

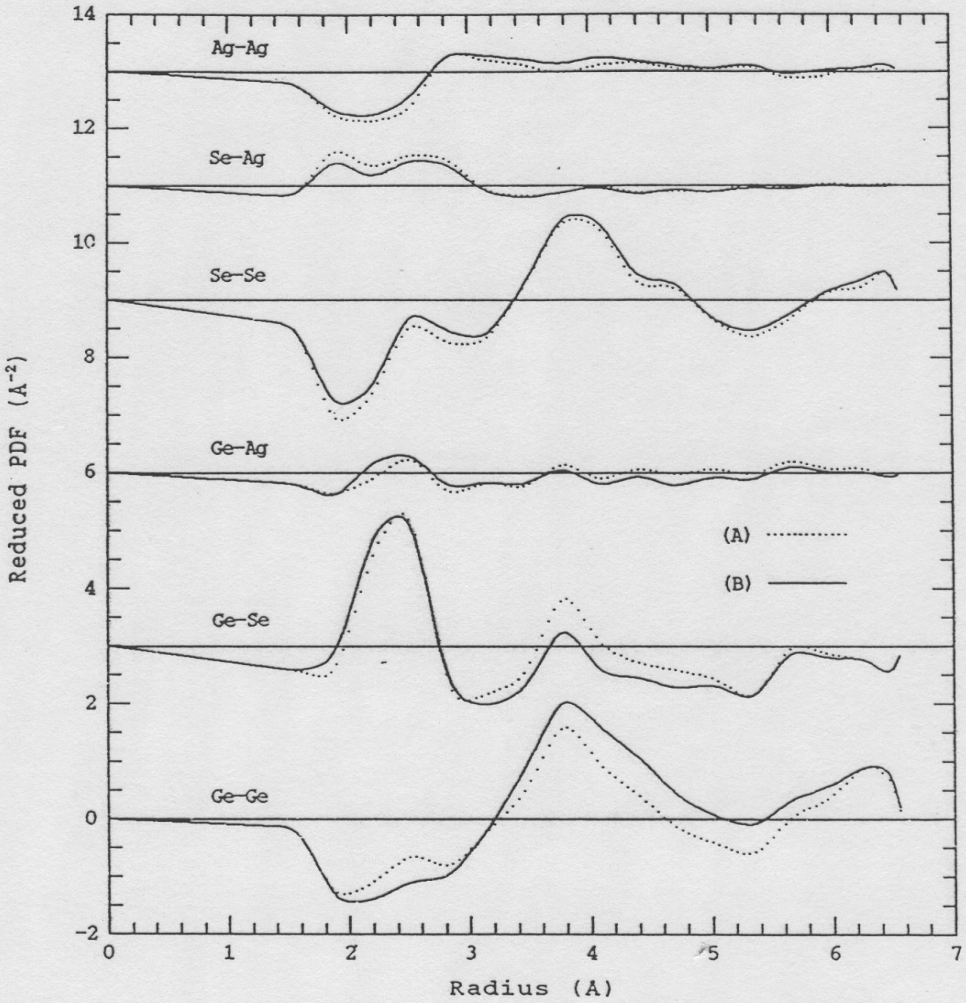

Figure 76: Comparison of MEM Results for Two Equivalent Sets of Input Data. The set of results (A) has been obtained using the scans at 11000, 11099, 12554, 12658, 25300, and 25500 eV as input data. The (B) set has been calculated using the scans at 11000, 11104, 12554, 12654, 25300, and 25500 eV. The vertical scale is shifted for each function.

TABLE 17

Summary of MEM PDF Results

Atom at Origin	Neighbor	First Shell Radius (Å)	First Shell Area	Second Shell Radius (Å)	Second Shell Area
Ge	Ge	2.54	-1.25 (?)	3.79	6.2
	Se	2.44	3.95	3.79	8.6
	Ag	2.49	0.53	3.79	...
Se	Ge	2.44	1.32	3.79	2.37
	Se	2.57	-0.78 (?)	3.89	14.1
	Ag	2.60	2.09	...	...
Ag	Ge	2.49	0.40	3.79	...
	Se	2.60	4.70	...	...
	Ag	2.91 (?)	1.42 (?)	...	...

The RDF and the DDF's are related to the PDF's by

$$RDF = \sum_{\alpha=1}^{M} X_\alpha DDF_\alpha = \sum_{\alpha=1}^{M} X_\alpha \sum_{\beta=1}^{M} PDF_{\alpha\beta}$$

Nucleation and crystallization behavior of glass-ceramic materials in the Li_2O-Al_2O_3-SiO_2 system

The ternary system Li_2O-Al_2O_3-SiO_2 is know to give transparent glass ceramic materials with low thermal expansion coefficient and high mechanical properties.

The mechanical properties are improved by a high crystalline fraction.

If the size (<40nm) of the crystallites is much smaller of the visble wave length the material is transparent.

The technological solution to the problem of obtaining high crystallinity and small crystallites is to modify the glass composition introducing a small amount of nucleating oxides that develop a large numbers of very small nuclei. These nuclei have to be developed by a thermal treatment carried out at a temperature lower than the crystallization one.

The main phases constituting the glass will crystallize on these nuclei during a second thermal treatment. A large number of nuclei allow to obtain a high crystallinity degree and small crystallites.

	I	II
SiO_2	60.8	66.9
Al_2O_3	19.4	20.5
Li_2O	4.85	3.45
BaO	3.2	1.00
ZrO_2	4.10	1.80
TiO_2	3.10	2.50
Sb_2O_3	1.92	//
ZnO	1.00	0.80
As_2O_3	//	0.80
P_2O_5	1.00	//

Glass composition wt%

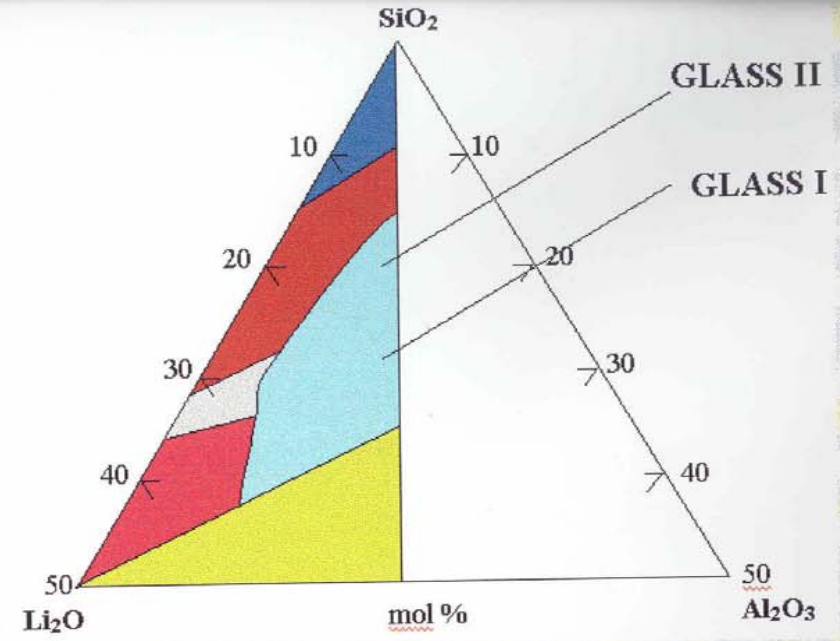

TERNARY PHASE DIAGRAM AND EQUILIBRIUM STRUCTURES

- CRYSTOBALITE
- TRYDIMITE
- LITHIUM DISILICATE
- LITHIUM METASILICATE
- β-EUCRYPTITE
- β-SPODUMENE

THE NUCLEATION STAGE
953 K 20h

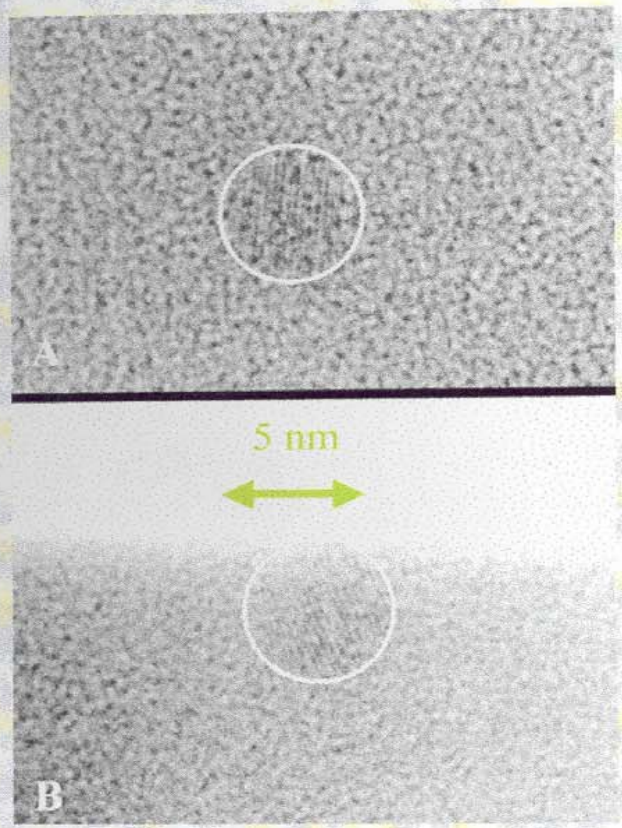

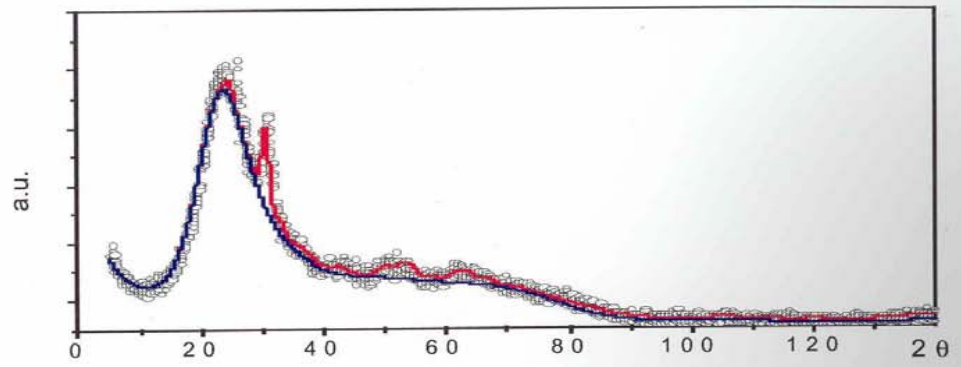

- $ZrTiO_4$ nucleated phase
- Amorphous phase (smoothed)

The nucleated glass shows the peaks of small $ZrTiO_4$ nuclei.

The crystallite size determined by the peak broadening analysis is 4.0±0.6 nm.

The weight fraction obtained by Rietveld analysis is m=4.3wt% [1]

The nuclei concentration determined by X ray diffraction is: $C_n = 7.8\ 10^{16}$ nuclei/cm^3[3]

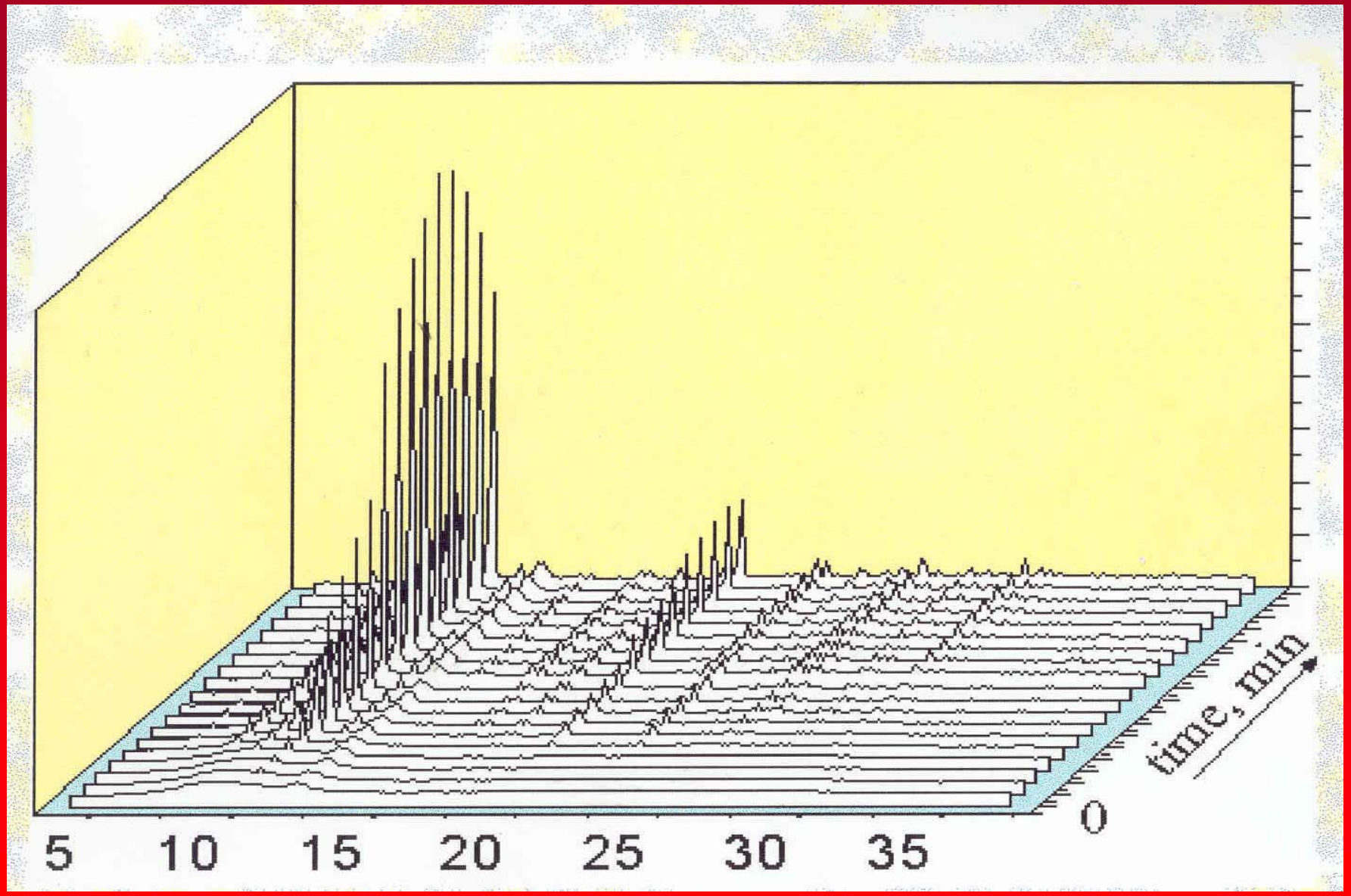
5
10
15
20
25
30
35
0
time, min

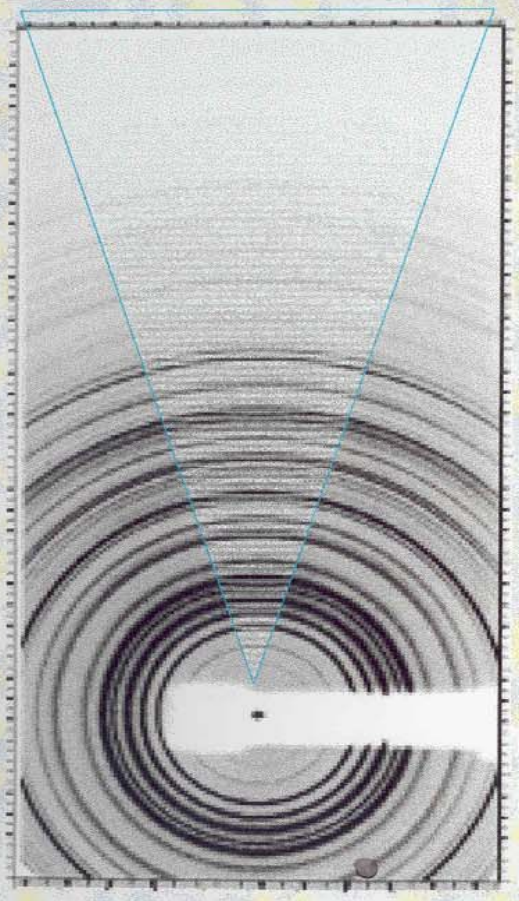

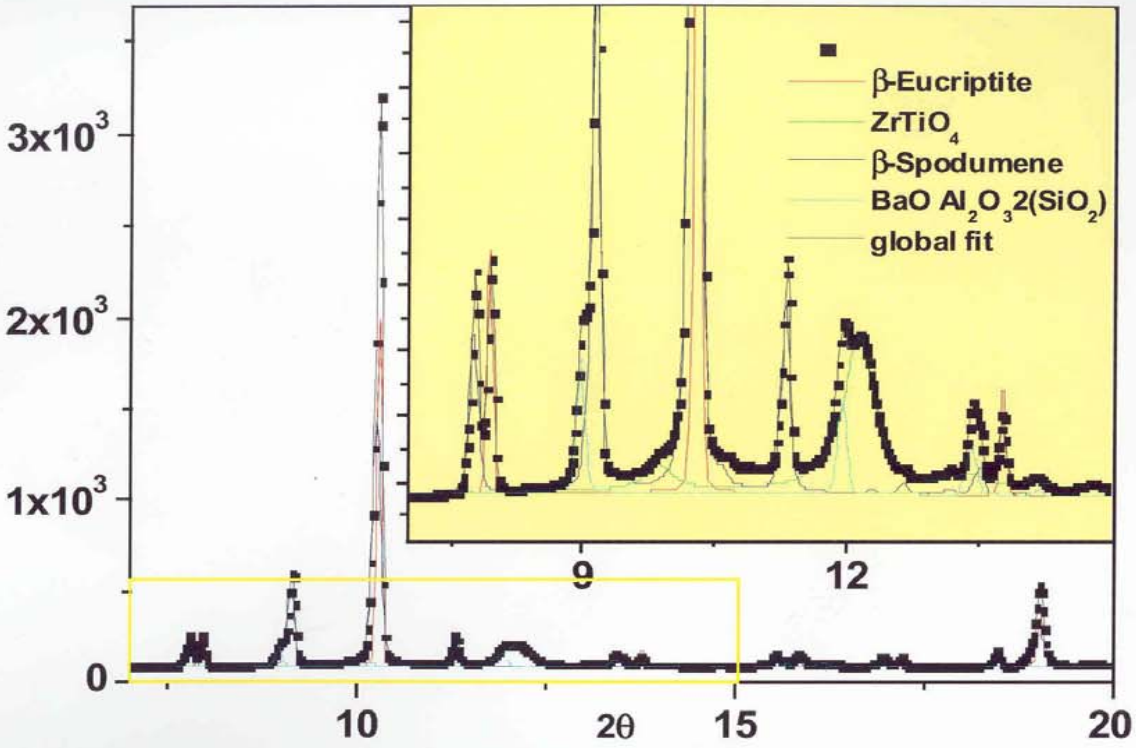
β-Eucriptite
ZrTiO4
β-Spodumene
BaO Al2O3 2(SiO2)
global fit
3x10^3
2x10^3
1x10^3
0
9
12
10
2θ
15
20

GLASS I

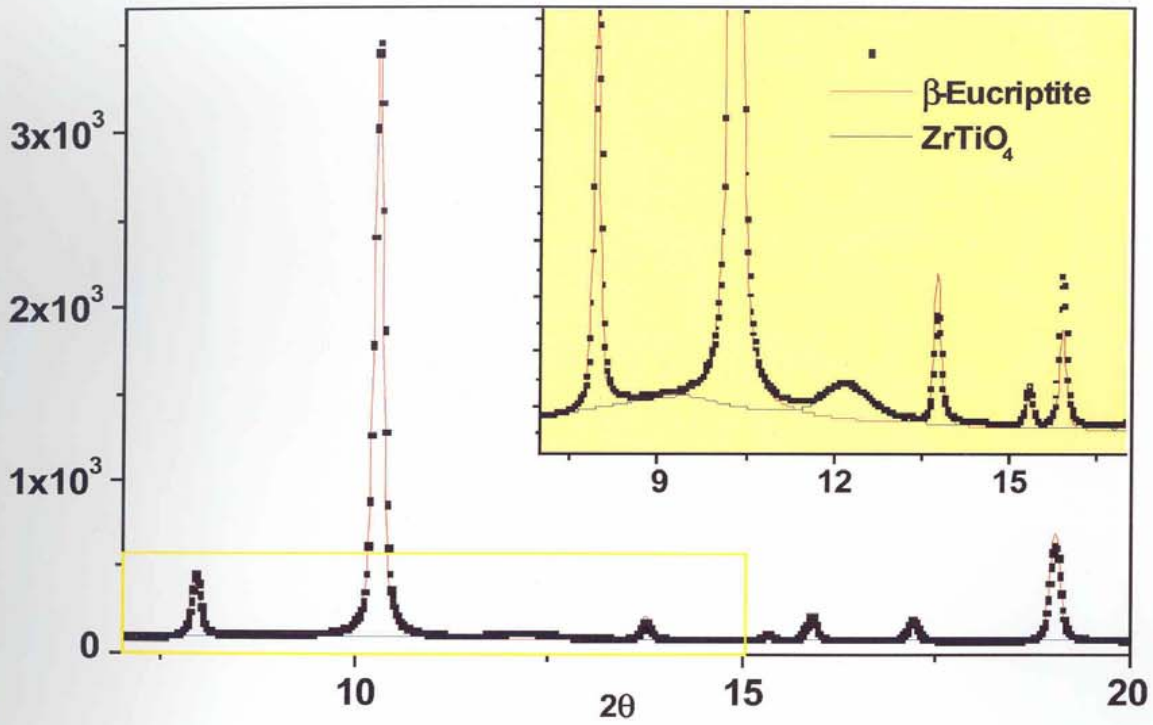

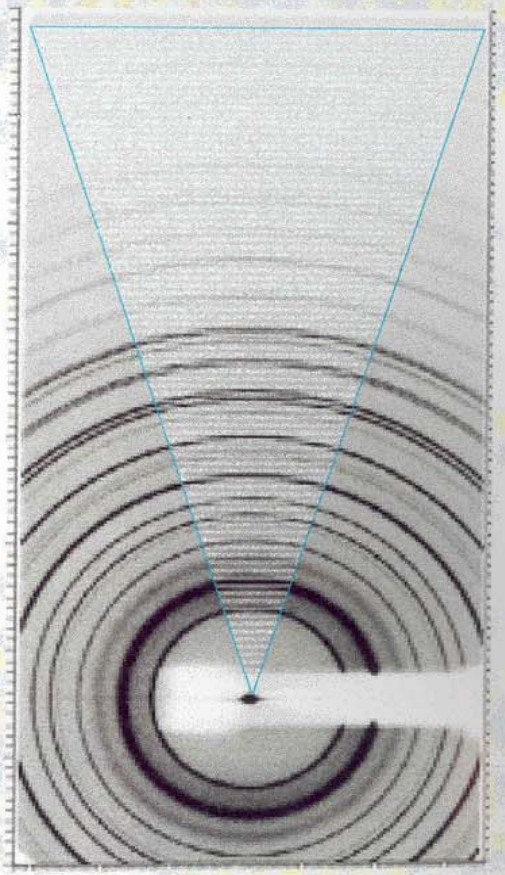

GLASS II

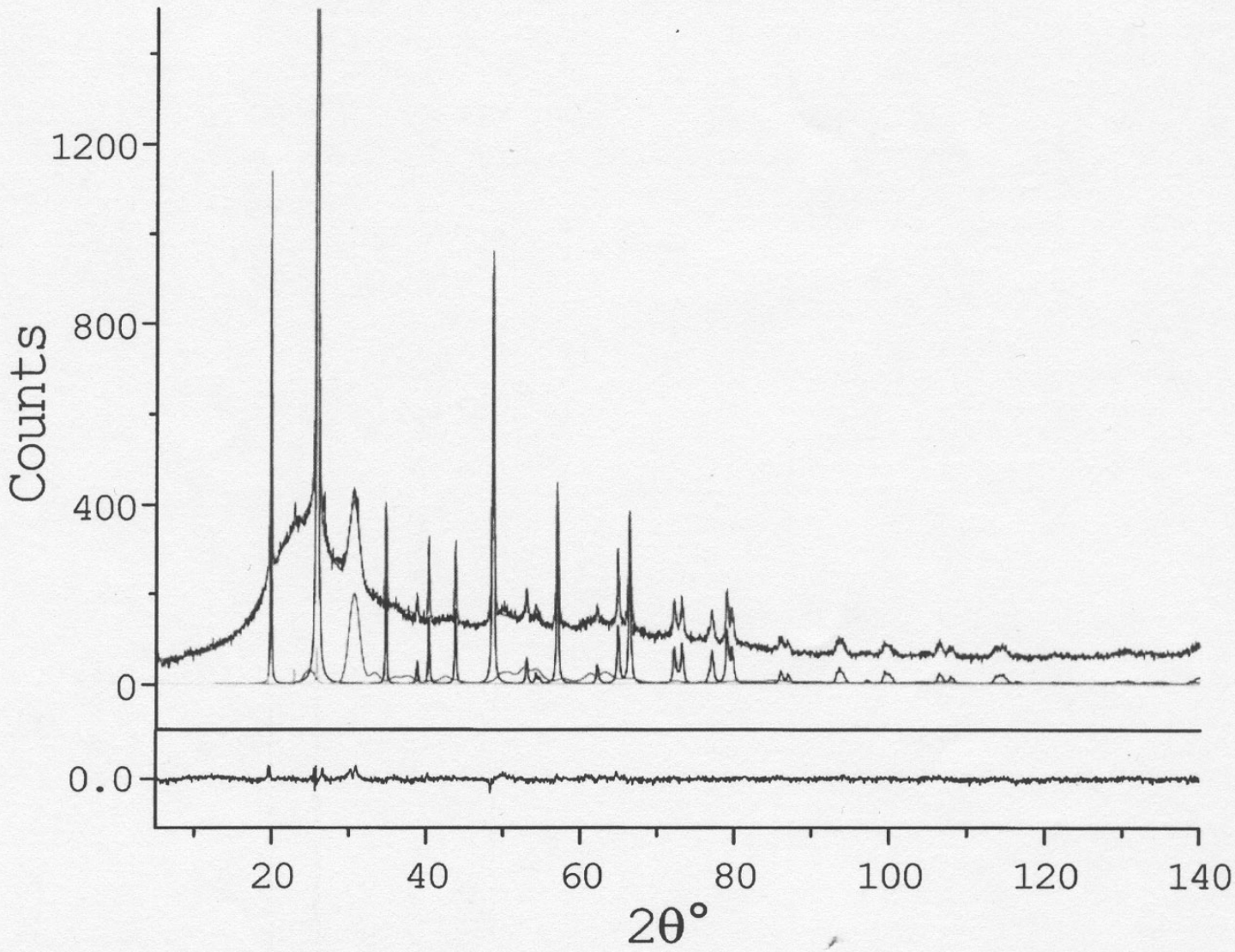

Fig. 5. XRD pattern (black line) of the glass-ceramic specimen, heated at 1023 K for 1.5 h. The continuous line represents the global Rietveld fit (crystalline phases plus the different contributions to the diffuse scattering), while the XRD peaks of the three crystalline phases: $ZrTiO_4$ (red line), β-eucryptite (blue-line) and β-spodumene (pink-line) are shown, for reasons of clarity, as fictitiously arising from a zero background line. The weighted residuals are also indicated. The goodness of fit, S, is 1.4.

Table 1
Quantitative analysis (mass%) of the crystal phases developed by heating the glass (nucleated at 953 K) at 1003 and 1023 K for different lengths of time, as determined with the Rietveld method

Phase	Crystal phase mass percentage								
	1003 K					1023 K			
	3.5 h	6.5 h	10.5 h	12 h	24 h	0.5 h	1.5 h	3.5 h	19.5 h
β-eucryptite s.s.	3.4	63.3	73.1	70.9	46.0	5.2	34.2	57.5	6.2
β-spodumene s.s.	n.d.[a]	0.6	4.2	5.6	34.5	n.d.[a]	1.4	22.7	72.4
$ZrTiO_4$	4.3	13.9[b]	13.7[b]	13.6[b]	11.2	5.4	6.6	12.6[b]	10.0
$BaAl_2Si_2O_8$	n.d.[a]	n.d.[a]	n.d.[a]	0.4	5.9	n.d.[a]	n.d.[a]	n.d.[a]	7.1

The relative percentage error in the Rietveld determination of minor crystalline phases can be evaluated from about ±20% to about ±10%, while this error can decrease to about ±5% for the major phases. [a] Not detectable (below the sensitivity limit of the technique). [b] These values for $ZrTiO_4$ appear clearly overestimated (beyond the estimated error of about ±15% of the method). This could be due to the fact that the determination of this phase is biased by the presence of low amounts of $BaAl_2Si_2O_8$, some peaks of which are partially superimposed on the titanate peaks, so that the peaks attributable to this last phase had a stronger intensity with respect to their correct intensity. When the barium alumino-silicate phase increased, then its XRD pattern could be distinguished (and refined) from that of $ZrTiO_4$, so that the determined quantity of this last phase was closer to the expected value of 7.3 wt%.

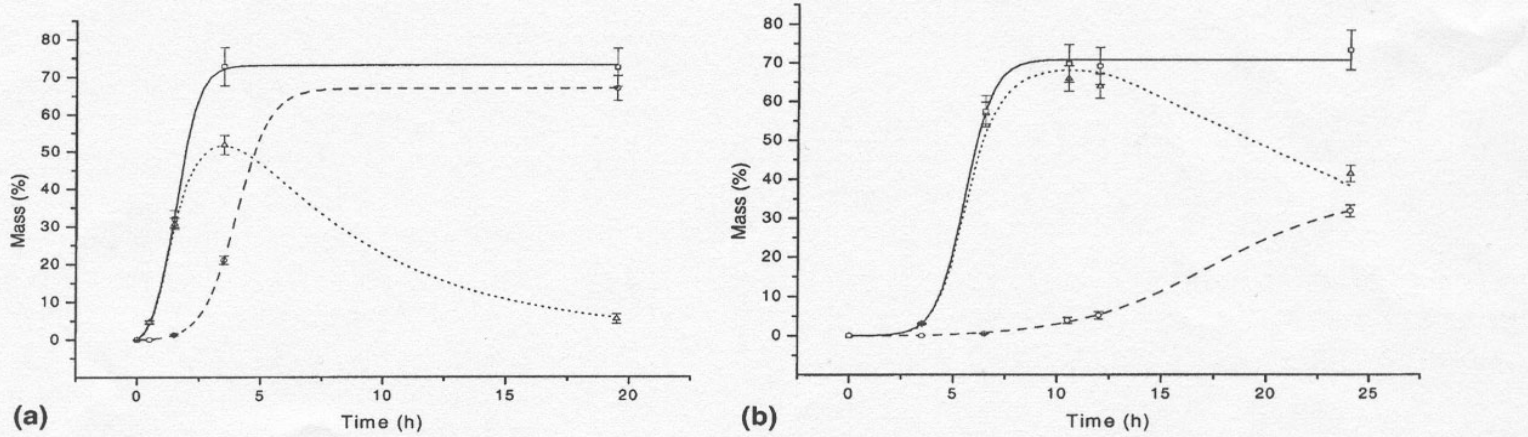

Fig. 7. The isothermal evolution of the crystallized mass, determined using the Rietveld method, of the two solid solutions at 1023 (a) and at 1003 K (b) is shown (β-eucryptite s.s.: triangles; β-spodumene s.s.: circles; sum of both phases: squares). The interpolated continuous lines were obtained by means of Avrami-like functions [24].

References

- "RESONANT ANOMALOUS SCATTERING" Edited by G.Materlik, C.J. Sparks and K. Fischer. North-Holland 1994.
- "Nucleation and crystallization behavior of glass-ceramics materials in the LiO2-Al2O3-SiO2 system of interest for their transparency properties. P.Riello et al. J. non-Cryst. Solids 288, 127 (2002).

Quantitative investigations of supported metal catalysts by ASAXS

Stefano Polizzi,[a]* Pietro Riello,[a] Günter Goerigk[b,c] and Alvise Benedetti[a]

[a]*Dipartimento di Chimica Fisica, Università Ca' Foscari di Venezia, Via Torino 155/b, 30170 Venezia-Mestre, Italy,* [b]*Institut für Festkörperforschung Forschungszentrum Jülich GmbH, Germany, and* [c]*HASYLAB (DESY), Hamburg, Germany. E-mail: polizzi@unive.it*

Limits and potentiality of anomalous small-angle X-ray scattering for the investigation of supported metal catalysts are discussed. The different sources of statistical errors are illustrated using two catalysts containing metals with absorption edges at very different energies (Au and Pd). Optimized experimental conditions and measuring strategy are proposed, and data-evaluation methods for obtaining quantitative reliable results are suggested. By this method, Au content as low as 0.2 wt% and Pd content of 3 wt% could be investigated with success. The detection limits for palladium are higher, mainly due to its smaller electronic contrast.

Keywords: ASAXS; methods; catalysis.

1. Introduction

Anomalous small-angle X-ray scattering (ASAXS) has been increasingly used over the last few years to study supported metal catalysts (Haubold & Wang, 1995; Haubold *et al.*, 1997; Benedetti *et al.*, 1997, 1999; Rasmussen *et al.*, 2000; Polizzi *et al.*, 2001) because of its ability to determine the size distribution of the active particles on a very convenient scale range, from nanoparticles of several tens of nanometres down to clusters of 1 nm. These kinds of catalysts are composed of an active metal phase dispersed in a porous support. The efficiency of the catalyst is increased by a good dispersion of the metal (no agglomeration or sintering) and by very small particles, since in this way the metal surface exposed to reagents is maximized.

ASAXS has proven to be able to provide essential quantitative information on these materials and is now considered an important technique in this field. However, the ASAXS data result from a small difference in the scattering at two energies, which is dependent on the particular metal and is obviously proportional to the amount of metal contained in the sample. Since industrial catalysts usually contain low metal fractions, the study of the detection limits of the ASAXS technique is of great interest.

In the present investigation, two cases are illustrated in detail: one catalyst containing Au and one containing Pd. Taking metals with absorption edges at very different energies was considered to represent a good choice to test the possibilities of ASAXS. The different sources of statistical errors are investigated and possible experimental improvements and appropriate evaluation methods are shown, with the aim of understanding, and possibly extending, the limits of the technique.

2. Theoretical background

For the simple case of homogeneous spherical metal particles with radius r in a homogeneous matrix, the small-angle scattering cross section per sample volume, V_s, can be written as (neglecting particle interference scattering) (Haubold & Wang, 1995; Haubold *et al.*, 1996)

$$\frac{d\sigma}{d\Omega_{Me}}(h, E) = \Delta\rho^2(E)\,\frac{N_{Me}}{V_s}\int_0^\infty P(r)V^2(r)S^2(h, r)\,dr, \qquad (1)$$

where N_{Me} is the number of metal particles and $h = 4\pi\sin\theta/\lambda$ is the modulus of the scattering vector with wavelength λ and scattering angle 2θ. $V(r)$ is the volume of a particle and $P(r)$ is the size distribution. $S(h, r)$ denotes the scattering function of a spherical particle (Guinier & Fournet, 1955). $\Delta\rho(E)$ is the energy-dependent electron density contrast between the metal particles and the surrounding matrix,

$$\Delta\rho(E) = \left|d_{Me}f_{Me}(E) - d_M f_M(E)\right|, \qquad (2)$$

where d_{Me} and d_M are the average atomic densities of the metal particles and of the matrix, respectively. f_{Me} are the atomic scattering factors of the metal, which in general is energy-dependent,

$$f_{Me}(E) = Z_{Me} + f'_{Me}(E) + if''_{Me}(E), \qquad (3)$$

where Z_{Me} denotes the number of electrons of the metal atoms and $f'(E)$ and $f''(E)$ are the so-called anomalous dispersion corrections. In the vicinity of the absorption edges of the metal, the atomic scattering factor of the metal particle shows strong variation (see, for example, Figs. 1 and 2), while the atomic scattering factor of the matrix atoms remains almost constant [$f_M(E) \simeq$ constant].

Applied to the situation of a sample containing metal particles in a matrix with a porous structure, for instance in a carbon or silica support, SAXS studies with a fixed X-ray energy, *e.g.* the characteristic radiation from an X-ray tube, do not allow one to separate the scattering of the metal particles from the scattering of the support material, because the pores represent a third phase (with zero electron density). In this case, the total scattering is a superposition of only two contributions† and is written as follows (Haubold & Wang, 1995; Haubold *et al.*, 1996),

$$\frac{d\sigma}{d\Omega_{total}}(h, E) = \frac{d\sigma}{d\Omega_{Me}}(h, E) + \frac{d\sigma}{d\Omega_M}(h). \qquad (4)$$

Owing to the weak energy dependence of f_M, which enters into $d\sigma/d\Omega_M$, the small-angle scattering of the matrix remains almost unchanged with energy, while the small-angle scattering of the metal particles changes strongly at energies near the absorption edge of the metal. Thus, the scattering of the metal particles can be obtained by subtraction of the small-angle scattering measured at the two energies E_1 and E_2,

$$\frac{d\sigma}{d\Omega_{total}}(h, E_1) - \frac{d\sigma}{d\Omega_{total}}(h, E_2) = \left[\Delta\rho^2(E_1) - \Delta\rho^2(E_2)\right]\frac{N_{Me}}{V_s} \times \int_0^\infty P(r)V^2(r)S^2(h, r)\,dr. \qquad (5)$$

Thus, the size distribution of metal particles can be easily obtained by using an analytical function for $P(r)$ and fitting the calculated scat-

† The cross term describing mutual correlations is neglected for the following reason. In metal-supported catalysts obtained by impregnation, metal particles are mostly deposited in pores with sizes significantly larger than the metal particles, since such pores are more easily filled by the liquid solution. In this case, if one imagines the metal particles distributed over the inner surface of the pores, the strong cross-correlation between pores and metal particles would give contributions to the scattering only at very small angles, outside the visibility range of the experiment. The cross-correlation of neighbouring pores would appear at even lower scattering angles.

tering intensities [the integral in (5)] to the experimental data by means of an optimization procedure.

If the experimental scattering intensities are scaled in absolute electron units, further quantitative results can be obtained from the scale factor $K = [\Delta\rho^2(E_1) - \Delta\rho^2(E_2)]N_{Me}/V_s$, which is an output of the optimization procedure. If the difference in electronic contrast is known, the volume fraction of the metal phase can then be determined, since $V_f = N_{Me}\langle V\rangle/V_s$, and the average particle volume, $\langle V\rangle$, can be calculated from the best-fit particle distribution $P(r)$ by $\langle V\rangle = \int P(r)(4/3)\pi r^3\, dr$. Furthermore, if the densities of the sample (d_s) and of the metal particles (d_m) are known, the obtained V_f can be compared with the weight fraction, V_w, obtained by atomic spectroscopy ($V_w = V_f\, d_m/d_s$), and can serve as a consistency test for the ASAXS evaluation procedure.

Yet, in the case of supported catalysts, the electron density contrast terms $\Delta\rho^2(E_i)$ are badly defined, because of the three-phase nature of these systems (metal, support, pores). In fact, while for the metal the electron density of the bulk metal can be used, the electron density of the matrix will be something between that of the bulk matrix and zero (pores). In some cases, such as noble metals on carbon, where the electronic density difference between metal and matrix is very high, this ambiguity does not lead to significant differences, so that Haubold & Wang (1995) could neglect the influence of the surrounding carbon. On the contrary, in the case of Pd/SiO_2 catalysts, different choices for the electron density of the matrix yield significant differences in the electron contrast and hence in the estimate of V_f.

Therefore, while anomalous scattering allows one to isolate the scattering of the metal phase and to overcome the difficulties related to the high porosity of the support, it does not always solve the problem of the quantitative determination of the metal content. However, the two limit cases can be worked out: (*a*) metal particles embedded in a bulk matrix, or (*b*) metal particles inside pores. In the first case the electron density of the bulk support (carbon or silica) is taken as a matrix, whereas in the second case a zero electron density is used. In this way, two values of V_f are obtained, which define a range where the actual value is predicted to be.

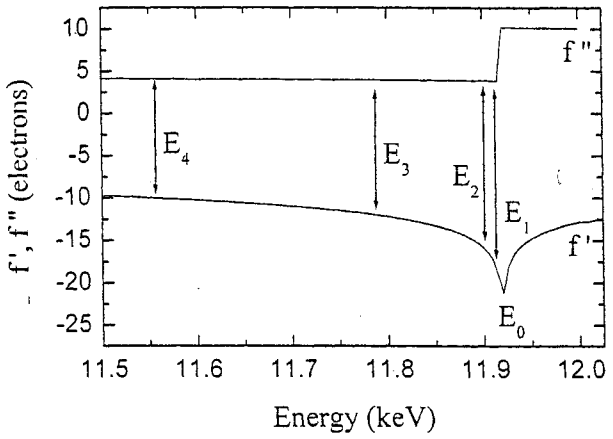

Figure 1
Energy-dependent anomalous dispersion corrections of the atomic scattering factor of Au, f' and f'', as a function of energy. The arrows show the energies at which measurements have been carried out (see Table 1 for energy values).

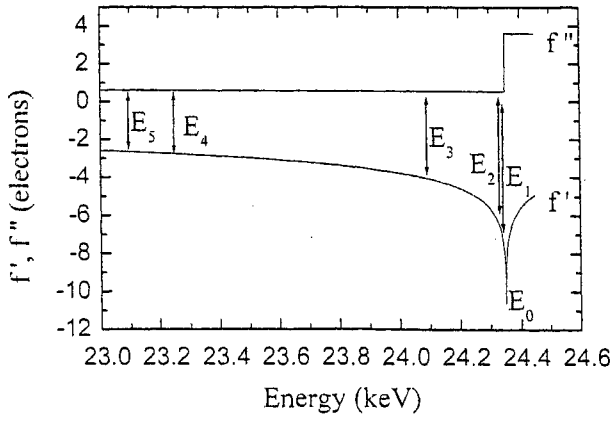

Figure 2
Energy-dependent anomalous dispersion corrections of the atomic scattering factor of Pd, f' and f'', as a function of energy. The arrows show the energies at which measurements have been carried out (see Table 2 for energy values).

3. Experimental

3.1. Sample preparation

For the Au sample, a commercial active carbon with a surface area of 1200 $m^2\ g^{-1}$ and a pore volume of 0.60 ml g^{-1} has been used as support. The catalyst was obtained by impregnation with an aqueous solution of $HAuCl_4$ and was reduced by HCOOH at 353 K. The Au content determined by atomic spectroscopy was 0.2 wt%.

The Pd sample was prepared by impregnation of SiO_2 (Akzo Chemie F22; surface area 400 $m^2\ g^{-1}$; particle size range 100–150 µm) with aqueous solutions of Na_2PdCl_4. After drying at 383 K for 18 h, samples were calcinated at 773 K for 1 h, then reduced at 623 K for 2 h and passivated (5% O_2 in Ar) before storing in air. The Pd content was 2.9 wt%, as determined by atomic spectroscopy.

3.2. ASAXS measurements

Measurements were performed at the JUSIFA small-angle scattering beamline of the DORIS synchrotron radiation source at DESY (Hamburg) (Haubold *et al.*, 1989). The contrast variation was performed at different energies (see Tables 1 and 2) near the Au L(III) (E_0 = 11918 eV) and the Pd K (E_0 = 24350 eV) absorption edges. The energies are also indicated in Figs. 1 and 2, which show the energy-dependent part of the atomic scattering factor calculated using the method of Cromer & Liberman (1970). Energies were calibrated using the measured K absorption edges of Se (12658 eV) and Au foils for the measurements of the Au-containing samples, and of the K absorption edges of Ru (22117 eV) and Pd foils for the Pd-containing samples.

Data were recorded using a two-dimensional gas-filled multiwire proportional counter, whose sensitivity map was determined by using an appropriate metallic foil (Se and Pd for measurements at the Au and Pd energies, respectively), and collecting for at least 12 h the isotropic fluorescence above its absorption edge and the small-angle scattering below it. By subtracting the latter from the former, a sensitivity map of the detector was obtained at the desired energy, which was used to correct the collected two-dimensional data. The dark current of the detector was measured at the beginning of the experimental session. Two-dimensional data were circularly averaged over rings at fixed h values in order to give one-dimensional curves with the same abscissa for different energies. In order to have direct control of the statistical errors and of the possible variation with time of the source characteristics, a large number (up to 16) of short runs (1–3 min each) were collected, evaluated and then averaged. The background scattering was measured before each run by moving the sample out of the incident beam. Sample transmission was measured

Table 1
Energy-dependent parts of the atomic scattering factor, f' and f'', near the Au L(III)-edge energy, E_0, at the energies where ASAXS measurements have been carried out.

In the last column the average transmission is shown with uncertainties in parentheses.

	E (eV) ± 2 eV	f'	f''	Transmission
E_1	11915	−19.062	3.889	0.619 (1)
E_2	11901	−16.052	3.896	0.619 (1)
E_3	11789	−12.018	3.957	0.615 (1)
E_4	11560	−10.006	4.085	0.596 (1)

Table 2
Energy-dependent parts of the atomic scattering factor, f' and f'', near the Pd K-edge energy, E_0, at the energies where ASAXS measurements have been carried out.

In the last column the average transmission is shown with uncertainties in parentheses.

	E (eV) ± 3 eV	f'	f''	Transmission
E_1	24346	−8.003	0.551	0.745 (2)
E_2	24343	−7.486	0.551	0.748 (2)
E_3	24084	−4.029	0.562	0.748 (2)
E_4	23269	−2.772	0.598	0.729 (2)
E_5	23090	−2.640	0.607	0.727 (2)

with an X-ray sensitive diode before and after each run for 1 min. Scattering from a reference scatterer (500 μm glassy carbon), used to calibrate the data in absolute units, was measured at the end of each run for 5 min. Data were normalized to the primary beam intensity and corrected for the different absorption coefficients.

For the Pd sample, measurements at a sample–detector distance of 2.735 m were sufficient to give the whole required angular range, whereas, for the Au sample, measurements at two different distances (0.935 m and 3.635 m) had to be matched.

In both samples studied, a single distribution of particles was not sufficient to describe the scattering intensity. For this reason a bimodal distribution was used,

$$P(r) = \left[P_1(r) + K_{\rm rel}P_2(r)\right]/(1 + K_{\rm rel}), \qquad (6)$$

where $K_{\rm rel}$ is the ratio of the total number of smaller particles to that of the larger ones and $P_i(r)$ are normalized Schulz distributions,

$$P(r) = \frac{1}{\Gamma(z+1)}\left(\frac{z+1}{\langle r\rangle}\right)^{(z+1)} r^z \exp\left(-\frac{z+1}{\langle r\rangle}r\right), \qquad (7)$$

where z (with $z > -1$) is the form parameter of the distribution (Riello & Benedetti, 1997).

Particles have been described by a spherical shape on the grounds of experimental considerations on the sample preparation procedure, which is likely to produce approximately spherical particles, and on TEM images (Polizzi *et al.*, 2001). Yet, this particular choice does not affect the main features of the final results (Brumberger *et al.*, 1996).

The catalyst powder was manually pressed into a cylindrical hole (6 mm diameter) of a metal sample holder and sealed with a non-scattering tape. A small lateral hole (2 mm), filled with a filter, connected the inner hole to the evacuated chamber. The sample thickness was 4 mm for both catalysts.

4. Results and discussion

A general experimental problem encountered with the investigated materials is related to the preparation of samples for the ASAXS measurements. Since metal-supported catalysts are usually powders, it is very important that the sample is mechanically stable during measurements. It was found that the pressure exerted under vacuum by the air trapped inside the powder was large enough to cause a visible swelling of the tape and rearrangement of the powder. This can change the density of the scattering material and the measured transmission, introducing errors in the data analysis. For this reason the original sample holder was modified by making a small lateral hole filled with a filter through which the trapped air can escape during chamber evacuation. Judging from the measured absorption values (see later), this sample holder seems to solve the problem of the sample stability.

The ASAXS signal is the difference between two measurements at two different energies, which are necessarily taken at a different time. When samples with small metal fractions are to be investigated, one is forced to increase the statistic quality of the data and to reduce as much as possible fluctuations in all experimental parameters that can occur during the collection time. To this aim, a measuring strategy consisting of the reiteration of short runs was considered to be much more appropriate than that of simply counting for longer times. Using a strategy of short-time runs, one is able to monitor all experimental variables (transmission, background, reference sample for the calibration of the scattering curves into absolute units) before and after each measurement, and to control the statistics of the experiment. It is clear that, for example, a short possible instability in the synchrotron incoming beam (position or intensity) would average in an integral measurement, whereas in a multiple-runs experiment such a fluctuation can be identified and the relevant run discarded. On the basis of the authors' experience, this is a very important check in a synchrotron radiation experiment, which uses highly complex instrumentation, and particularly in an ASAXS measurement, which is based on small differences owing to the energy dependence of the scattering intensity. Reiterate measurements of the transmission of the sample provide an idea of the stability, both of the sample itself and of the incoming beam. Since data are normalized to the energy-dependent transmission, this value must have an uncertainty at least smaller than the signal difference at the two energies studied, which is dependent on the difference in f' and on the metal content. In Figs. 3 and 4, transmission values (one before and one after each measurement) of different runs are shown for the four energies used near the Au absorption edge and for two different energies near the Pd edge (only two energies are shown for clarity in this case). In Tables 1 and 2 all average values are reported with their relevant uncertainties. The standard deviation of the transmission values is usually smaller than 1% of the measured values, so that averaging over ten runs (20 transmission values) yields an uncertainty lower than 0.2% (slightly higher for the Pd samples). The difference due to the change in energy is close to the statistical error for the energies in the neighbourhood of the edge, but it is clearly visible for most distant energies.

A further factor whose precision is crucial is the scaling factor for absolute intensity. This factor is calculated from the plateau present in the scattering intensity of a reference sample (glassy carbon), which is previously calibrated using a rotating anode. Thus, the scaling factor is a measure of the primary beam intensity and, in fact, a direct correlation was found with the incoming intensity measured using a NaJ detector. However, strongly diverging values were often found during the first half hour after injection of a new synchrotron beam, probably owing to a settlement of the beam position. The intensity of a synchrotron beam is continuously decreasing with time, so that measurements of the glassy carbon must be as close as

possible in time to that of the sample, but measurements too close to a new injection should be discarded. The measuring strategy proposed in this work allows the former condition to be satisfied and a few measurements to be discarded with a minimum waste of beam time.

Short-time oscillations of the incoming beam could also give rise to errors in the value of the measured transmission, since this is determined by two successive intensity measurements (with and without sample). However, with the adopted measuring strategy, the influence of such instabilities is reduced, and, in fact, no correlation was found between transmission values and the factor for absolute intensity, which should exclude this kind of error.

Let us finally look at the statistical errors on the curves obtained as an average of the different experimental runs by comparing curves at different energies. In order to have a direct indication of the real experimental errors, each run was evaluated separately. Averages and standard deviations were then worked out for each single data point of all scattering curves measured at the same energy. In Fig. 5 the average scattering intensities of eight runs for the two most distant energies (E_4 and E_1) measured at the longer sample–detector distance is shown for the Au-containing sample, together with the relevant standard deviations of the average. The difference between the two curves is very small, but the insets show that they are clearly separated by more than one standard deviation, at least until h values of about 1.6 nm^{-1}, and tend to overlap only in the very end of the angular range, where the intensity is very small. The curve obtained by subtracting the E_1 curve from the E_4 curve (the subtracted curve) with error bars calculated from the relevant standard deviations and the best-fit with equation (1) has already been published in an earlier paper (Benedetti *et al.*, 1997, 1999). It is important to note that the scattering difference obtained by other energy pairs gradually decreased with decreasing energy difference, showing the reliability of the data. Two different populations of particles were found from the quantitative analysis of these curves: one with average diameters of 14 nm and the other consisting of small particles with an average size of 2 nm. Furthermore, a very interesting finding was that the small particles are an overwhelming majority, being three times the weight of the larger ones. Even if these values are subjected to large errors, because the scattering owing to small particles takes place at larger h values where the data are less accurate, the presence of a large population of particles smaller than 3 nm has been confirmed by a later study using Rietveld analysis (Riello *et al.*, 1998.) The total weight fraction has now been calculated and is compared with the value obtained by atomic absorption in Table 3. As explained in the

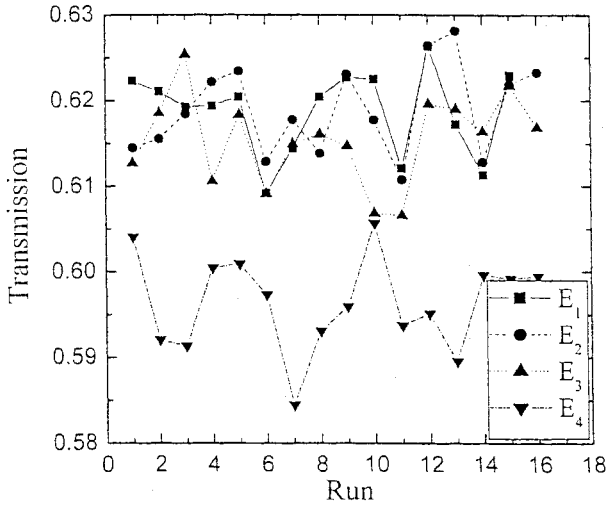

Figure 3
Transmission values of the Au(0.2 wt%)/C sample measured before and after each of eight different experimental runs at different energies near the Au absorption edge.

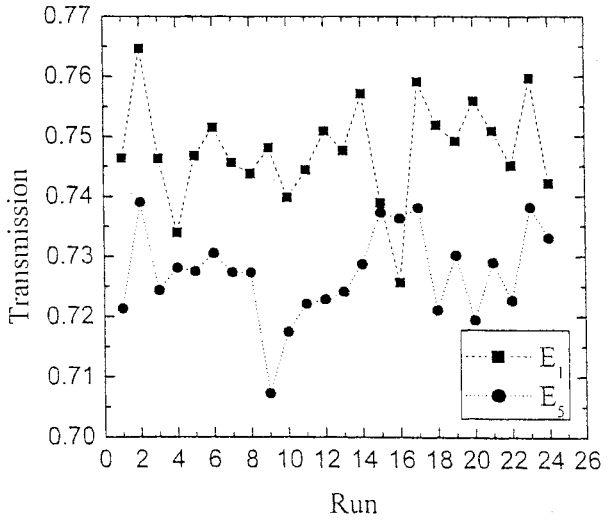

Figure 4
Transmission values of the Pd(2.9 wt%)/SiO_2 sample measured in the different experimental runs at different energies near the Pd absorption edge. Only two energies are shown for clarity.

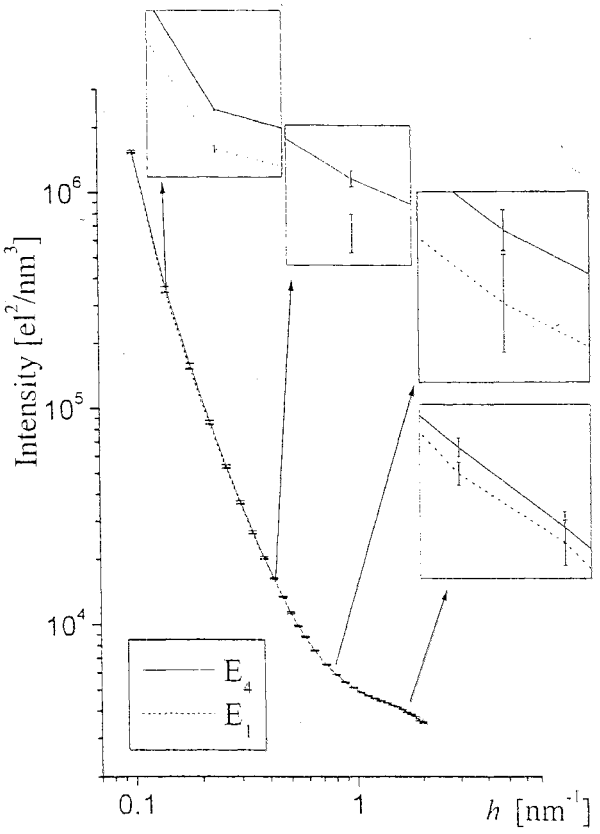

Figure 5
Scattering curves of the Au(0.2 wt%)/C sample at two different energies (E_1 and E_4, sample–detector distance = 3.635 m). Insets show different enlarged regions.

theoretical section, the range of values indicated for the ASAXS result indicates the two limit assumptions for the electron density of the matrix. It can be seen that the uncertainty due to the latter choice is small and that the ASAXS value agrees with the result obtained by atomic absorption.

Discussing now the measurements of the Pd-containing samples, it must be noticed that, from the experimental point of view, measurements at the Pd edge present some further problems in addition to those encountered at the Au edge.

First, the difference in the scattering factor at two different energies close to the Pd K edge is quite small: the highest difference at the measured energies is just 5.4 electrons, in contrast to the 9 electrons at the Au L(III) edge. This means that the signal level is much lower and that the sensitivity to Pd of the technique is almost half of that for Au.

Also, the energy resolution of the monochromator at JUSIFA is $\Delta E/E < 2 \times 10^{-4}$, so that at the Pd edge an uncertainty of the order of a few eV can be expected.

In Fig. 6 the two scattering curves for the Pd-containing sample for E_1 and E_5 obtained by averaging over 12 runs are shown together with the relevant standard deviations. It can be seen that data are separated by more than one standard deviation, at least until h values of about 2 nm^{-1}, and that at higher h values a crossover of the curves occurs. Such a crossover has already been described in similar measurements (Schliermann *et al.*, 2000) and can be due to different effects such as a very small residual fluorescence background close to the absorption edge, to second-order (mixed terms) resonant scattering or to a special electronic configuration (*e.g.* oxide film).

The final subtracted curve is shown in a double logarithmic scale in Fig. 7, together with error bars and the best-fit obtained using equation (1). Notwithstanding the large uncertainties and the aforementioned experimental problems, the final results that are drawn from this curve are quite reasonable and in very good agreement with the findings of other techniques (TEM, WAXS, EXAFS, absoprtion spectroscopy), as shown elsewhere (Polizzi *et al.*, 2001). The main results of this analysis were: (i) the presence of two populations of particles with average values of 3 nm and 13 nm; (ii) smaller particles represent some 80% of the whole metal; (iii) quantitative analysis of the Pd content gave 2.7 (4) wt%, in accordance with the value obtained by atomic spectroscopy (see Table 3). Again, the range of the ASAXS value indicates the two limit assumptions for the electron density of the matrix. The uncertainty in the quantitative determination for the Pd sample is larger than for the Au sample because the difference between the electronic density of the metal and that of the support is smaller for Pd and silica than for Au and carbon. One could think that the best value to be used for evaluating the electronic density contrast should be the average electronic density of the sample. Yet, with this choice a metal content of 2.4% was found, whereas the atomic absorption value was much

Table 3
Total metal fraction obtained by atomic absorption and by SAXS.

The range indicated in the ASAXS results refers to two different choices for the electron density of the matrix (see text).

Sample	Atomic absorption	ASAXS
Au/C	0.20 (1) wt%	0.18%–0.21%
Pd/SiO_2	2.9 (2) wt%	2.3%–3.1%

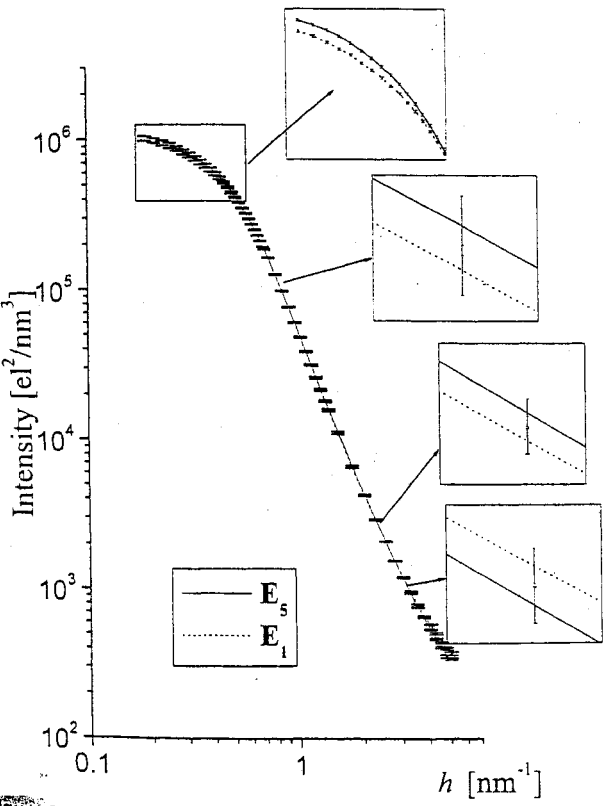

Figure 6
Scattering curves of the Pd(2.9 wt%)/SiO_2 sample at two different energies. Insets show different enlarged regions.

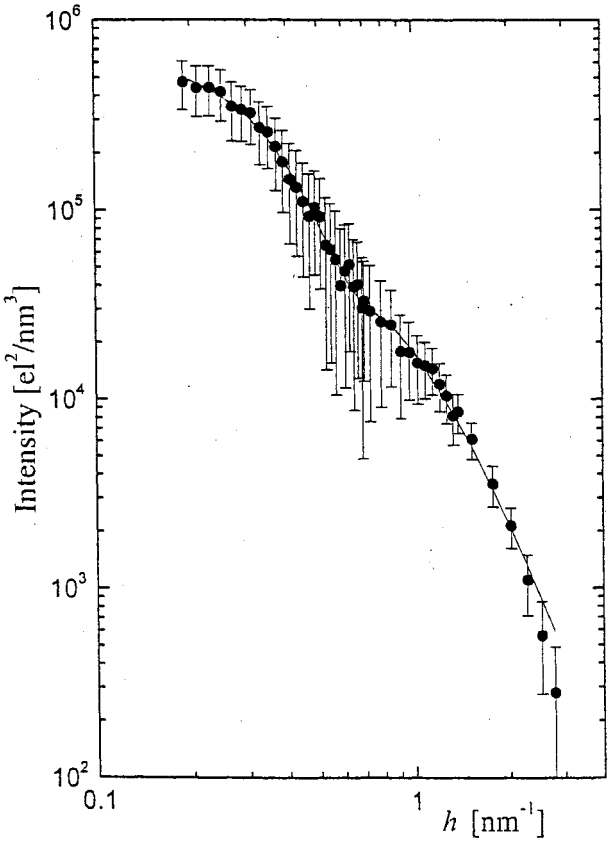

Figure 7
Final scattering curve of the Pd(2.9 wt%)/SiO_2 sample in a double logarithmic plot. The continuous line is the best-fit obtained using equation (1).

closer to the value obtained using the electronic density of bulk silica. Apparently, metal particles are, on average, surrounded more by silica than by pores.

5. Conclusions

It was shown that a measuring strategy consisting of reiterated short-time runs with frequent control of the experimental parameters is recommendable in the case of metal-supported catalysts with low metal load in order to reach a sufficient control of the statistics of the data. By this method, gold content as low as 0.2 wt% and palladium content of 3 wt% could be investigated with success. The detection limits for palladium are higher, mainly due to its smaller electronic contrast.

This work was supported by the TMR Contract ERBFM-GECT950059 of the European Community. Financial support from 60% MURST is also acknowledged. The authors are grateful to one of the referees for his/her sharp remark concerning equation (4), that inspired the footnote.

References

Benedetti, A., Bertoldo, L., Canton, P., Pinna, F., Goerigk, G., Riello, P. & Polizzi, S. (1999). *Catal. Today*, **49**, 485–489.
Benedetti, A., Polizzi, S., Riello, P., Pinna, F. & Goerigk, G. (1997). *J. Catal.* **171**, 345–348.
Brumberger, H., Goodisman, J., Ramaya, R. & Ciccariello, S. (1996). *J. Appl. Cryst.* **29**, 526–530.
Cromer, D. T. & Liberman, D. (1970). *J. Chem. Phys.* **53**, 1891–1898.
Guinier, A. & Fournet, G. (1955). *Small-Angle Scattering of X-rays*, p. 19. New York: Wiley.
Haubold, H.-G., Gruenhagen, K., Wagener, M., Jungbluth, H., Heer, H., Pfeil, A., Rongen, H., Brandenburg, G., Moeller, R., Matzerath, J., Hiller, P. & Halling, H. (1989). *Rev. Sci. Instrum.* **60**, 1943–1946.
Haubold, H.-G. & Wang, X. H. (1995). *Nucl. Instrum. Methods Phys. Res. B*, **97**, 50–54.
Haubold, H.-G., Wang, X. H., Goerigk, G. & Schilling, W. (1997). *J. Appl. Cryst.* **30**, 653–658.
Haubold, H.-G., Wang, X. H., Jungbluth, H., Goerigk, G. & Schilling, W. (1996). *J. Mol. Struct.* **383**, 283–289.
Polizzi, S., Riello, P., Balerna, A. & Benedetti, A. (2001). *Phys. Chem. Chem. Phys.* **3**, 4614–4619.
Rasmussen, F. Berg, Molenbroek, A. M., Clausen, B. S. & Feidenhans, R. (2000). *J. Catal.* **190**, 205–208.
Riello, P. & Benedetti, A. (1997). *J. Chem. Phys.* **106**, 8660–8663.
Riello, P., Canton, P. & Benedetti, A. (1998). *Langmuir*, **14**, 6617–6619.
Schliermann, T., Glora, M., Pröbstle, H., Petričević, R. & Fricke, J. (2000). HASYLAB Annual Report, pp. 449–450. HASYLAB, DESY, Hamburg, Germany.

 Received 15 November 2001 · Accepted 16 January 2002

ELSEVIER

Journal of Non-Crystalline Solids 288 (2001) 127–139

JOURNAL OF NON-CRYSTALLINE SOLIDS

www.elsevier.com/locate/jnoncrysol

Nucleation and crystallization behavior of glass-ceramic materials in the Li_2O–Al_2O_3–SiO_2 system of interest for their transparency properties

P. Riello [a], P. Canton [a], N. Comelato [a], S. Polizzi [a], M. Verità [b], G. Fagherazzi [a,*], H. Hofmeister [c], S. Hopfe [c]

[a] *Dipartimento di Chimica Fisica, Università di Venezia, DD2137, I-30123 Venezia, Italy*
[b] *Stazione Sperimentale del Vetro, Via Briati 10, I-30141 Murano-Venezia, Italy*
[c] *Max Planck Institut of Microstructure Physics, Weinberg 2, D-06120 Halle, Germany*

Received 20 June 2000; received in revised form 1 March 2001

Abstract

We investigated the nucleation and crystallization behavior of multi-phase glass-ceramic materials (in the Li_2O–Al_2O_3–SiO_2 system to which low amounts of oxides such as TiO_2, ZrO_2, P_2O_5, BaO, Sb_2O_3 and ZnO were added), with interest in their transparency properties as glazes for industrial tiles with high scratch resistance. X-ray diffraction (XRD) and transmission electron microscopy (TEM) were used. XRD showed that the nucleating oxides produce, during the nucleation stage (at 953 K for 20 h), an orthorhombic $ZrTiO_4$ phase, which maintains a similar crystallite size (about 4 nm) during the subsequent crystallization processes. We succeeded in determining the concentration of nuclei by using XRD data only. This quantity resulted close enough to the corresponding one, determined using the classical TEM method. The formation of each crystalline phase, developed during the crystallization stage, as a function of the thermal treatment, was quantitatively measured using the Rietveld method. In particular, the isothermal transformations at 1003 and 1023 K of the characteristic main phase, i.e., β-eucryptite s.s., which is richer in silica with respect to the relevant stoichiometric phase, into β-spodumene s.s., also richer in silica, were found to be consecutive solid state reactions. Moreover, this preliminary investigation aims at improving knowledge of the mechanisms leading to the development of transparent/opaque materials during the thermal treatment of Li_2O–Al_2O_3–SiO_2 glass-ceramics.

1. Introduction

The ternary system Li_2O–Al_2O_3–SiO_2 is known [1–6] to give transparent glass-ceramic materials with low linear thermal expansion characteristics. In order to investigate the possible applications in the field of glazes for industrial tiles with high scratch resistance, we performed a structural study on the nucleation and crystallization stages of this system. The composition of the as-quenched glass was chosen for this study after having tested many other similar compositions in previous exploratory researches. The quantities used for the three main oxides were measured systematically in fairly large intervals, between 55 and 62 wt% for SiO_2, between 12.5 and 20 wt% for Al_2O_3 and between

* Corresponding author.
E-mail address: fagheraz@unive.it (G. Fagherazzi).

0022-3093/01/$ - see front matter
PII: S0022-3093(01)00518-X

5 and 10.5 wt% for Li_2O. To these main oxides some nucleating oxides (TiO_2, ZrO_2, P_2O_5), and other modifiers (BaO, Sb_2O_3, ZnO) were added in small amounts. As is known, such oxides are important for catalyzing the nucleation process, as well as for different technological purposes, as explained in Section 2. However, it was not completely clear in the literature which phases these oxides could form inside the Li_2O–Al_2O_3–SiO_2 system. The aim of this paper was the detection, as well as the structural and microstructural investigation, of the crystalline phases formed during the nucleation or crystallization stages, using X-ray diffraction (XRD) and transmission electron microscopy (TEM) techniques. In particular, with the XRD technique, by means of an 'ad hoc' tailored Rietveld method, already used by us in microstructural studies of several semi-crystalline materials [7] one aim was to determine quantitatively the observed crystalline phases, in order to investigate the transformation kinetics of the first phase, formed during the crystallization stage (i.e., the β-eucryptite solid solution) to β-spodumene solid solution, and to determine the stoichiometry of both phases.

A technological aim of this work was to crystallize large amounts of β-eucryptite (during the primary crystallization) with small crystallite size ($\leqslant 50$ nm), in order to achieve the required transparency properties [5], and to avoid the formation of bigger crystals of β-spodumene (formed during the secondary crystallization, at higher temperatures and/or at longer periods of isothermal treatment).

Since nucleation is very important in controlling the crystallization process, in order to obtain a fine microstructure, another purpose was to make a comparison between the nuclei concentrations, when directly obtained by TEM and, indirectly, from the combined XRD data. Finally, a differential thermal analysis (DTA) was employed, in order to establish the temperatures for the nucleation and crystallization isothermal treatments.

High wear resistant tiles with an opaque, rough surface are already produced using the Li_2O–Al_2O_3–SiO_2 glass-ceramic system associated to other glass frits. This research is a part of the preliminary work aimed at investigating the possibilities of obtaining tiles with similar mechanical properties, but having a shiny, bright surface, possibly on a transparent or translucent glaze.

2. Experimental and methodological section

2.1. Glass preparation and heat treatments

The composition in wt% of the as-quenched glass, chosen for this study, after having tested many other similar compositions in previous exploratory researches, was: SiO_2(60.8), Al_2O_3(19.4), Li_2O(4.9), TiO_2(3.1), ZrO_2(4.2), P_2O_5(1), BaO(3.2), Sb_2O_3(1.9), ZnO(1.0). These percentages were determined using X-ray fluorescence spectroscopy and analytical chemical methods. TiO_2, ZrO_2 and P_2O_5 were introduced as nucleating agents, BaO and ZnO to reduce the melting temperature of the batch and to improve the glass workability, while Sb_2O_3 was used as a refining agent.

The thermal treatments of nucleation and crystallization (carried out in two separate stages) were performed on bulk pieces of glass, having a developed planar surface, appropriate for a qualitative and fast XRD investigation, carried out in the usual reflection mode. In order to eliminate, from the diffraction patterns, the possible effects due to surface crystallization, the sample surface was suitably abraded after heat treatment, before the XRD analysis. For the heat treatments we used a tubular furnace, electronically controlled to reach ±1 K of excursion during the isothermal stages. Since the technological aim of this work was to crystallize the β-eucryptite in high quantities with a crystallite size of the order of 50 nm, thus avoiding the formation of bigger crystals of β-spodumene, in order to achieve the required transparency properties, the crystal growth at an isothermal temperature was established at two temperatures low enough with respect to the observed DTA peak maximum, i.e., at 1003 and 1023 K at several different times (see Table 1, where the quantitative Rietveld analysis is given). This also allowed us to follow the kinetic isothermal development of the different crystallized phases.

Table 1
Quantitative analysis (mass%) of the crystal phases developed by heating the glass (nucleated at 953 K) at 1003 and 1023 K for different lengths of time, as determined with the Rietveld method

Phase	Crystal phase mass percentage								
	1003 K					1023 K			
	3.5 h	6.5 h	10.5 h	12 h	24 h	0.5 h	1.5 h	3.5 h	19.5 h
β-eucryptite s.s.	3.4	63.3	73.1	70.9	46.0	5.2	34.2	57.5	6.2
β-spodumene s.s.	n.d.[a]	0.6	4.2	5.6	34.5	n.d.[a]	1.4	22.7	72.4
$ZrTiO_4$	4.3	13.9[b]	13.7[b]	13.6[b]	11.2	5.4	6.6	12.6[b]	10.0
$BaAl_2Si_2O_8$	n.d.[a]	n.d.[a]	n.d.[a]	0.4	5.9	n.d.[a]	n.d.[a]	n.d.[a]	7.1

The relative percentage error in the Rietveld determination of minor crystalline phases can be evaluated from about ±20% to about ±10%, while this error can decrease to about ±5% for the major phases.[a] Not detectable (below the sensitivity limit of the technique). [b] These values for $ZrTiO_4$ appear clearly overestimated (beyond the estimated error of about ±15% of the method). This could be due to the fact that the determination of this phase is biased by the presence of low amounts of $BaAl_2Si_2O_8$, some peaks of which are partially superimposed on the titanate peaks, so that the peaks attributable to this last phase had a stronger intensity with respect to their correct intensity. When the barium alumino-silicate phase increased, then its XRD pattern could be distinguished (and refined) from that of $ZrTiO_4$, so that the determined quantity of this last phase was closer to the expected value of 7.3 wt%.

In the case of the Rietveld XRD analysis, the bulk crystallized samples were finely powdered, in order to avoid preferred crystalline orientations.

DTA experiments were carried out under the following conditions: heating rate 10 K/min; sensitivity 0.1 mV for full scale expansion; 200 mg of sample vs. 200 mg of alumina in specimen holders of sintered alumina.

2.2. X-ray techniques and methods

The XRD patterns were recorded at 295 K, with a step size of 0.05°, on a 5–140° 2θ range. The intensities were collected in the preset-time mode (10 s). A system, equipped with a focusing graphite monochromator on the diffracted beam and with a proportional counter with an electronic pulse height discrimination, was used. Moreover, a divergence slit of 0.5°, a receiving slit of 0.2 mm., an anti-scatter slit of 0.5°, and Ni-filtered CuKα radiation (30 mA, 40 kV), were employed.

The Rietveld program used by us was a modified version of the DBWS-9600 code written by Sakthivel and Young [8]. In contrast to the traditional approach, which describes the background intensity by means of some analytical functions, our approach [9,10] separates the main different background components, giving a physical meaning to each of them. Neglecting the contribution due to the (very weak) polychromaticity, the incident beam is essentially constituted by the characteristic CuKα doublet (the presence of the monochromator, the filter and the pulse discrimination justifies this assumption). In absence of fluorescence the background components are: (1) the Compton scattering, which can easily be calculated when the chemical composition of the phases is known; (2) the air scattering (also containing the instrumental parasitic background), which must be suitably subtracted before the refining procedure; (3) the diffuse scattering caused by the thermal (plus static, if present) disorder of the atoms contained in the crystal phases; and, finally, (4) the scattering due to the amorphous phase.

As a result of this approach, it is possible to separate the single phase contributions to the diffraction pattern, including the diffuse scattering belonging to the crystalline phases. The global experimental intensities, $I^{\exp}$, to which air scattering, I^{air}, was suitably subtracted, can thus be divided into the following components:

$$I^{\exp}(s) - I^{\text{air}}(s) = I^{\text{am}}(s) + \sum_l \sum_k I_l^k(s), \qquad (1)$$

where $s = 2\sin(\theta)/\lambda$, with 2θ the Bragg diffraction angle and λ the wavelength; I^{am} is the amorphous contribution (if present) to the global scattering, and I_l^k is the intensity of the kth peak of the lth crystalline phase. I^{am} was obtained from a

reference (completely amorphous) sample and suitably scaled. In the present case the amorphous phase is constituted by the as-quenched glass itself, before the nucleation step.

The main advantage of this approach results from the Fourier transform properties of the global integrated intensity on the reciprocal space. In fact, such an integral depends only on the kind and quantity of atoms in each phase and is independent of their atomic spatial order (or disorder) [11].

Therefore, for a phase containing $N = Nn$ atoms, it is possible to write

$$\begin{aligned}\int_0^\infty I^{\mathrm{corr}}(s)4\pi s^2\,\mathrm{d}s &\propto \sum_{i=1}^{N}\int_0^\infty \left[|f_i^o|^2 + I_i^{\mathrm{inc}}\right]4\pi s^2\,\mathrm{d}s \\ &= N\sum_{i=1}^{n}\int_0^\infty \left[|f_i^o|^2 + I_i^{\mathrm{inc}}\right]4\pi s^2\mathrm{d}s, \end{aligned} \tag{2}$$

where we have supposed that the N atoms can be organized in N composition units, for instance the unit cells of the crystalline phases, each one composed of n atoms.

The symbols here used are: I^{corr} is the powder diffracted intensity, corrected for the absorption, polarization and air scattering of each phase or of the global sample, f_i^o is the tabulated atomic scattering factor of the ith atom, and I_i^{inc} is the incoherent scattering of the ith atom.

It is important to take into account that Eq. (1) can be applied to the crystalline phases intensities, as obtained by the Rietveld refining procedure, if such intensities are evaluated including their own thermal diffuse scattering.

The Rietveld equation in 2θ (measured step by step), including the diffuse background, which adequately describes the diffraction intensity $Y^{\mathrm{cr}}(2\theta)$ of a single crystalline phase and respects the integral theorem given by Eq. (2), is

$$\begin{aligned}Y^{\mathrm{cr}}(2\theta) &= KA(2\theta)P(2\theta) \\ &\times \left\{\sum_{k=1}^{n_B} J_k L_k |F_k|^2 \Phi(2\theta - 2\theta_k) + Y^{\mathrm{bk}}\right\},\end{aligned} \tag{3}$$

where [9,10]

$$\begin{aligned}Y^{\mathrm{bk}} &= (16\pi^2 V_c)/(180\lambda^3) \\ &\times \sum_{i=1}^{N}\left[I_i^{\mathrm{inc}} + [1 - \exp(1 - (2B\sin^2(\theta)/\lambda^2)]|f_i^o|^2\right]\end{aligned} \tag{3a}$$

with K being the scale factor, n_b the number of observed reflections, V_c the unit cell volume, $A(2\theta)$ the correction factor for absorption, $P(2\theta)$ the polarization factor (depending also on the monochromator set-up), J_k the multiplicity factor of the kth reflection, L_k the Lorentz factor $\frac{1}{\sin^2(\theta_k)\cos(\theta_k)}$, $|F_k|^2$ the squared structure factor for the kth reflection, including the Debye–Waller factor, $\Phi(2\theta - 2\theta_k)$ the normalized profile function describing the profile of the kth reflection, and B is the overall thermal factor.

When, in a multi-phase sample, it is possible to separate the contribution $Y_l^{\mathrm{cr}}(s)$ of the lth phase to the global scattering pattern, it is then possible to obtain the relative weight fraction, W_l, of the lth phase, if the chemical compositions of this phase and of the global sample are known [7,13]. In fact, N_l (number of composition units in the lth phase) and N_{global} (total number of composition units in the sample) are given by

$$\begin{aligned}CN_l &= \frac{\int_0^\infty \frac{Y_l^{\mathrm{cr}}}{AP}s^2\,\mathrm{d}s}{\sum_{i=1}^{n_l}\int_0^\infty \left[|f_i^o|^2 + I_i^{\mathrm{inc}}\right]s^2\,\mathrm{d}s}, \\ CN_{\mathrm{global}} &= \frac{\int_0^\infty \frac{Y_{\mathrm{global}}^{\mathrm{exp}} - Y^{\mathrm{air}}}{AP}s^2\,\mathrm{d}s}{\sum_{i=1}^{n_{\mathrm{global}}}\int_0^\infty \left[|f_i^o|^2 + I_i^{\mathrm{inc}}\right]s^2\,\mathrm{d}s}.\end{aligned} \tag{4}$$

Therefore W_l is given by

$$W_l = \frac{N_l\sum_{i=1}^{n_l} w_l^i}{N_{\mathrm{global}}\sum_{i=1}^{n_{\mathrm{global}}} w_{\mathrm{global}}^i}, \tag{4a}$$

where C is a constant, n_l and n_{global} are the number of atoms of the chosen composition unit and of the irradiated overall sample, where w_l^i and w_{global}^i are the atomic or molecular weights of the ith atom of the lth phase, or of the overall composition, respectively; A and P are the absorption and polarization factors, respectively, for which the measured intensities must be corrected. Note that in the ratio Eq. (4a) the C constant disappears.

From the operative point of view, the value of the ratios Eq. (4) can be estimated by the mean value of $CN_l(s_p)$ in the range of $s_p > 1.0$ Å^{-1}, i.e., $CN_l = \lim_{s_p \to \infty} CN_l(s_p)$, with

$$CN_l(s_p) = \frac{\int_{s_{\min}}^{s_p} \frac{Y_l^{cr}}{AP} s^2 \, ds}{\sum_i^n \int_{s_{\min}}^{s_p} \left[|f_i^o|^2 + I_i^{inc} \right] s^2 \, ds}, \quad (5)$$

where s_m corresponds to the initial measurement angle, which must be as low as possible.

By using this procedure, it is possible to measure the amounts of crystalline phases present in the glass-ceramic materials, without having the need for adding an internal standard powder to the sample. The air scattering, necessary in order to correct the measured intensities, was collected (10 s step^{-1} and step size of 0.5°) on the same 2θ range, fitted with a suitable function (two pseudo-Voigt functions and a straight line) and corrected in accordance with the method published elsewhere [12], taking into account the presence of the sample.

The average sizes of the crystallites were obtained by the use of the Fourier method, applied to the analytical diffraction peak profiles, which are couples of constrained pseudo-Voigt functions (describing the $K\alpha_1$–$K\alpha_2$ doublets), as has been explained elsewhere [14,15]. The volume-weighted average crystallite sizes $\langle D \rangle_{hkl}$, measured perpendicularly to the (hkl) lattice planes, were determined in correspondence with the hkl peak profiles, suitably chosen for each investigated crystal phase (usually the most intense among the most isolated reflections), as indicated in Section 3. The Fourier transforms of the measured peak profiles were corrected for instrumental broadening, using the very narrow diffraction lines of a reference standard sample (α-quartz). The peak broadening was attributed to crystallite size effects only.

2.3. TEM observations

The TEM measurements were carried out using a conventional transmission microscope operating at 100 kV and a high resolution electron microscope operating at 400 kV. The HRTEM images were recorded using optimal conditions (near Scherzer focus) on a photographic film and then digitized using a CCD video-camera. Particles were counted automatically using an appropriate software program (Scion Image), after having enhanced the contrast by imposing a suitable threshold. The samples for observation were obtained by means of conventional techniques, involving mechanical polishing, dimple grinding and Ar^+ ion beam etching.

3. Results

Fig. 1 shows the DTA trace, run on the as-quenched glass (trace (a)). Two exothermic peaks can clearly be seen, due to the crystallization of the β-eucryptite, with a maximum at about 1043 K and of the β-spodumene, with a maximum at about 1143 K. In order to choose an efficient nucleation temperature, three temperatures were tested: 933, 953 and 973 K for 20 h. In accordance with similar results reported by other authors [16,17], in Fig. 1 (traces (b), (c) and (d)) it is possible to see clearly a shift in the exothermic peak maxima towards lower temperatures as the preliminary nucleation heating treatment increases.

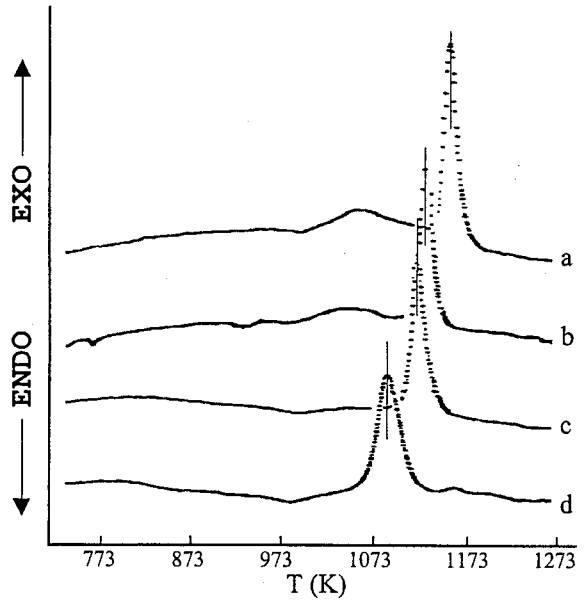

Fig. 1. DTA traces for the as-quenched glass (a), the glass nucleated at 933 K (b), the glass nucleated at 953 K (c) and the glass nucleated at 973 K (d), for 20 h.

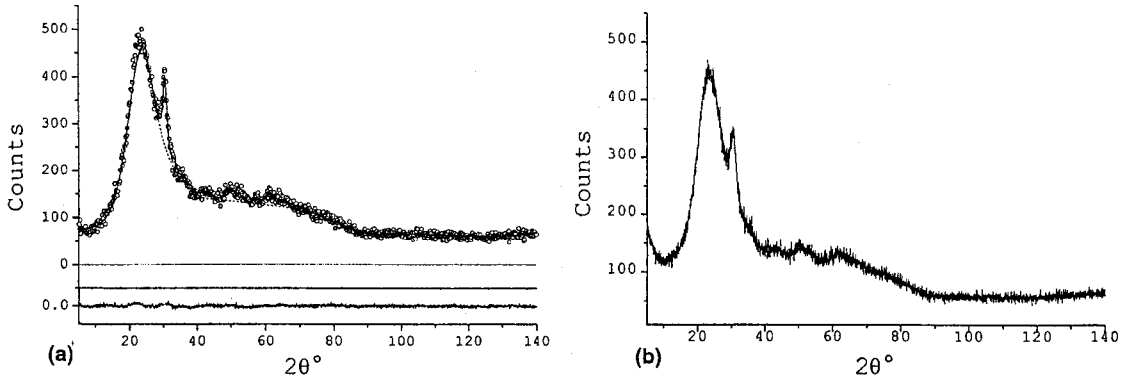

Fig. 2. XRD patterns of the glass nucleated at 953 K for 20 h (a) and of the glass nucleated at 933 K for 8 h (b). In the upper part of the figure the fitted global diffuse scattering is evidenced with a dashed line, which represents the sum of the smoothed experimental quenched glass, suitably scaled, the thermal diffuse scattering from the crystalline titanate phase, and Compton scattering. The weighted residuals, defined according to Young [25], are reported at the bottom of pattern (a). The goodness of fit S, also defined according to Young [25], is 1.2.

The broadening of the DTA main peak observed in trace (d), which corresponds to the glass sample nucleated at higher temperature (973 K), can be attributed to the fact that, at this temperature of nucleation, crystallization occurs, as detected by XRD. Therefore, the exothermic effects of the crystallization process tend to spread out toward lower temperatures.

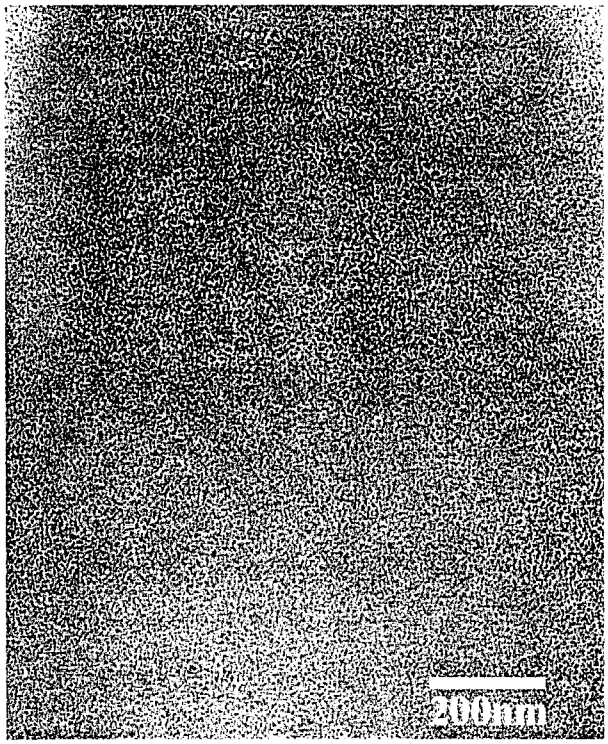

Fig. 3. Digitized TEM image of the nucleated glass (at 953 K for 20 h).

3.1. XRD and TEM investigations of the nucleation stage

Fig. 2 shows the XRD patterns of the glass nucleated at 953 K for 20 h (a) and, for comparison purposes, of the glass nucleated at 933 K for 8 h (b). In pattern (a), suitably fitted using our Rietveld method, a broad crystalline peak, centered at 30.55°, clearly appears, together with other broad and weak clusters of peaks, indicated with circles. Pattern (b) shows the same features, but with broader and lower peaks. Since the temperature of 973 K gave rise to a commencement of β-eucryptite s.s. crystallization, as shown by the XRD, the intermediate temperature of 953 K for 20 h was chosen as the standard nucleation temperature for all the subsequent crystallizations.

The Rietveld analysis, carried out on the glass nucleated for 20 h, confirmed that the $ZrTiO_4$ double oxide was formed (orthorhombic space group, Pbcn). The quantity determined using this analysis was 4.3 wt%, while in the glass the sum of the two reagent oxides was determined as 7.3 wt%, by means of the X-ray fluorescence technique. This discrepancy could be due to the fact

that not all the possible crystalline titanate phase were formed in the above-cited conditions of nucleation.

Fig. 3 shows a TEM image of the nucleated sample and Fig. 4 shows two HRTEM micrographs of the same sample with much higher magnification. In these images two single crystalline particles clearly appear, with structural features showing parallel fringes, due to the presence of lattice planes.

3.2. XRD investigation of the crystallization stage

$ZrTiO_4$ phase is present in all the glass-ceramic samples obtained during the crystallization stage. For example, at 1023 K for 1.5 h of thermal treatment, the amount of this phase was determined by the Rietveld analysis as 6.6 wt%, with the following unit cell parameters: $a = 0.484(1)$ nm, $b = 0.540(1)$ nm, $c = 0.502(1)$ nm. These values are similar to those found by Newnham [18] for an equimolar stoichiometry of the two component oxides. In particular, the unit cell volume of 0.1317 nm^3, as determined by the above-cited authors, was very close to that of 0.1312 nm^3, as found by us in this glass-ceramic sample.

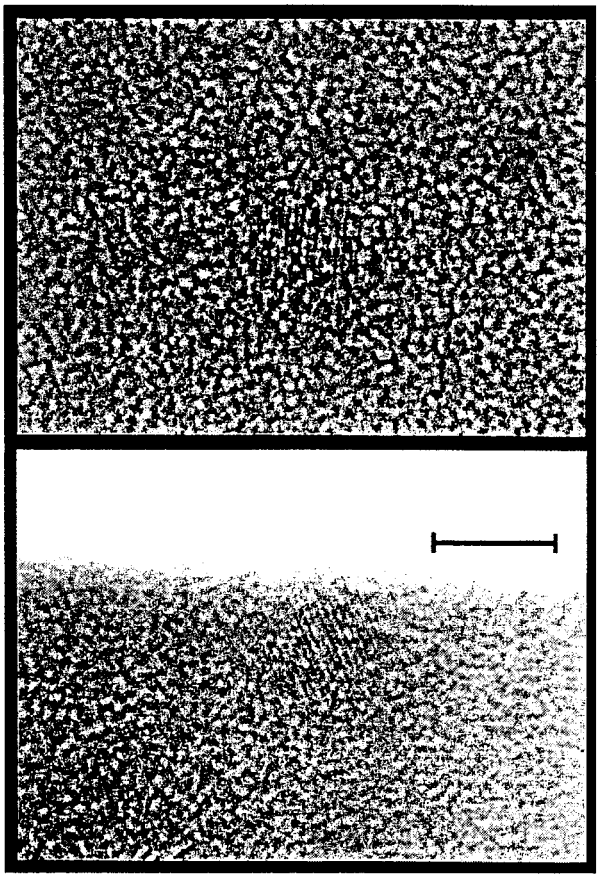

Fig. 4. Digitized HRTEM images showing two spheroidal crystalline nuclei of $ZrTiO_4$, embedded in the glassy matrix (sample nucleated at 953 K for 20 h). The bar corresponds to 5 nm.

Fig. 5 shows, as an example, the XRD pattern of the glass-ceramic specimen heated at 1023 K for 1.5 h (intermediate crystallization). It is interesting to note that the average sizes of the crystalline nuclei of $ZrTiO_4$ were found to be 4.3, 4.0 and 4.8 nm for the samples crystallized at 1023 K for 0.5, 1.5 and 3.5 h, respectively. All these values are close to that of 4.0 nm found for the nucleated glass, while the size increased to 9.5 nm for the sample crystallized at 1023 K for 19.5 h (the error for all the reported nuclei sizes is ±15%). This behavior is probably due to the fact that, during the crystallization stage, each nucleus remained isolated inside the β-eucryptite crystal which grows all around it, except for the final very long thermal treatment of 19.5 h, which causes an uncontrollable growth process in the titanate crystals.

As another example, Fig. 6 shows the Rietveld refinement of the XRD pattern of the glass-ceramic material, heated at 1023 K, for 19.5 h. A fourth crystalline phase then appeared, as elucidated in the two insets by means of circles (peak profiles colored in azure), i.e., $BaO \cdot Al_2O_3 \cdot 2SiO_2$, space group P6/mmm, $a = 0.5306(5)$ nm and $c = 0.7824(5)$ nm (unit cell edges obtained in the present refinement). The found amount of this phase was 7.1 wt%, measured using the Rietveld method. Furthermore, other very weak peaks appear, due to a fifth unknown phase (these peaks are indicated by yellow arrows in Fig. 6). As expected, in this sample the β-spodumene s.s. strongly increased, at the expense of the β-eucryptite s.s. (see Table 1). The titanate phase was measured as 10 wt%, a percentage higher than the already cited expected value of 7.3 wt%. However, the relative percentage error in the Rietveld determination of minor crystalline phases can be evaluated from about ±20% to about ±10%, while

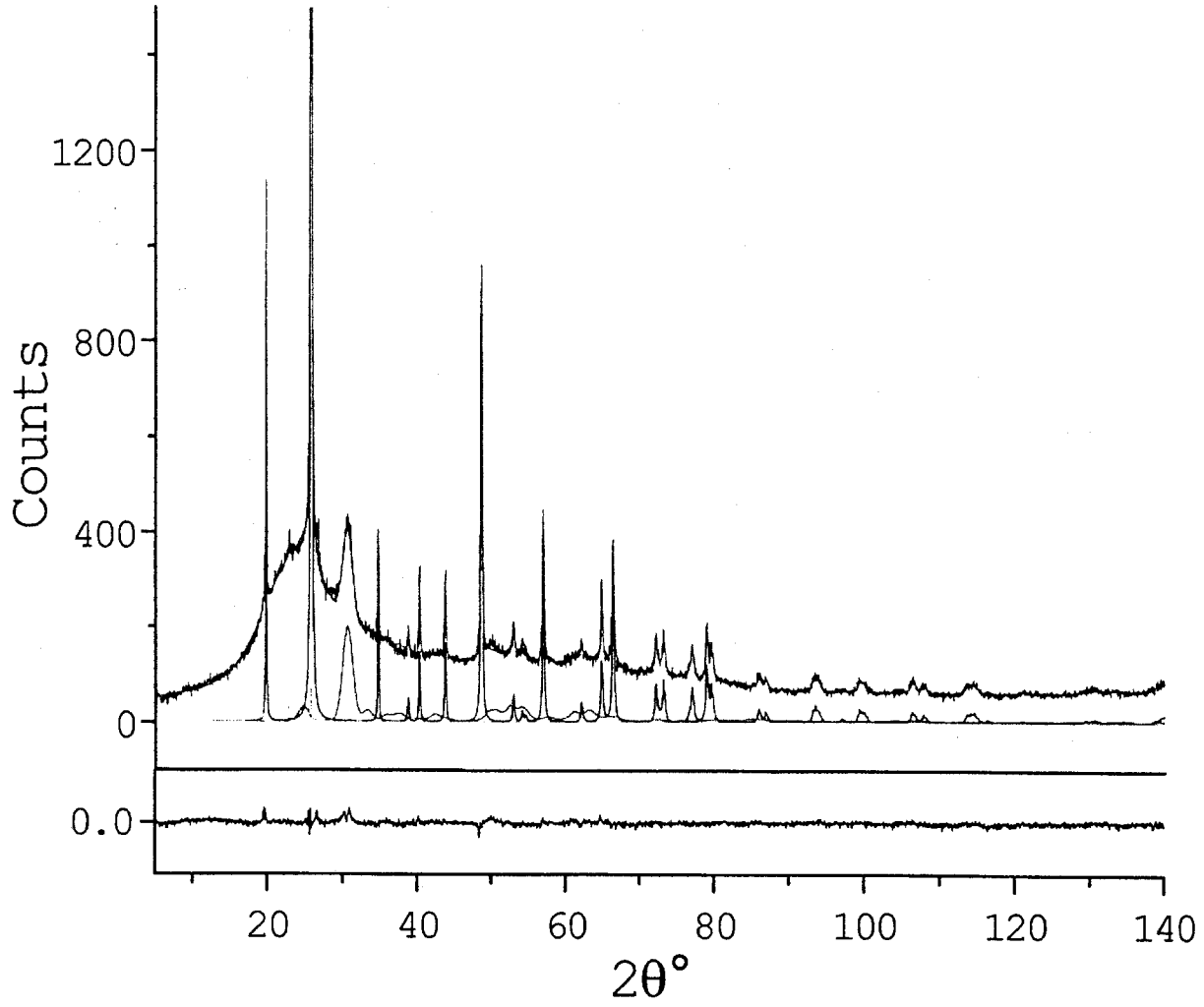

Fig. 5. XRD pattern (black line) of the glass-ceramic specimen, heated at 1023 K for 1.5 h. The continuous line represents the global Rietveld fit (crystalline phases plus the different contributions to the diffuse scattering), while the XRD peaks of the three crystalline phases: $ZrTiO_4$ (red line), β-eucryptite (blue-line) and β-spodumene (pink-line) are shown, for reasons of clarity, as fictitiously arising from a zero background line. The weighted residuals are also indicated. The goodness of fit, S, is 1.4.

this error can decrease to about ±5% for the major phases. Moreover, the fifth unknown crystalline phase could bias the quantitative analysis of the barium alumino-silicate phase. This sample, containing such a high quantity of β-spodumene, was completely opaque, while the samples rich in β-eucryptite gave good transparency properties.

Table 2 reports the unit cell parameters (with an average error evaluated as about ±0.0005 nm by the Rietveld refinement itself) obtained using the Rietveld method, for the two major phases, β-eucryptite s.s. (hexagonal space group $P6_222$) and β-spodumene s.s. (tetragonal space group $P4_32_12$).

3.3. Development and transformation of β-eucryptite to β-spodumene

Since the technological aim of this work was to crystallize the β-eucryptite s.s. in high quantity, with a crystallite size not higher than about 50 nm, and to minimize the formation of the β-spodumene s.s., in order to achieve the required transparency properties, the crystal growth at an

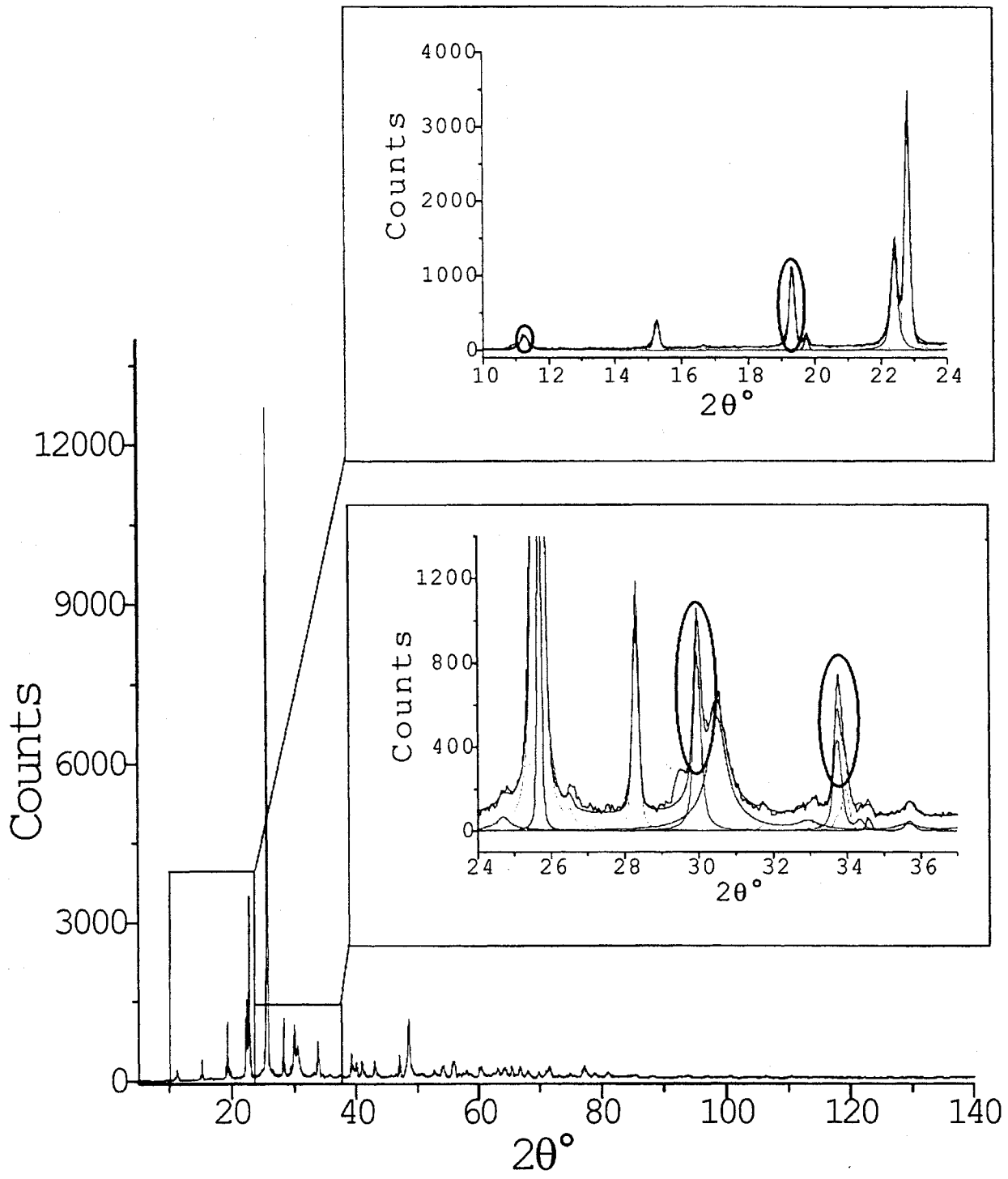

Fig. 6. XRD pattern of the glass-ceramic specimen, heated at 1023 K for 19.5 h (almost completely crystallized). The two insets illustrate the presence of the minor phases, i.e., $BaO \cdot Al_2O_3 \cdot 2SiO_2$ (peak profiles of an azure color) and the so-called unknown phase, indicated by yellow arrows. For other details see the text.

Table 2
Edges *a* and *c* (nm) of the unit cells of β-eucryptite s.s (hexagonal) and β-spodumene s.s (tetragonal), refined by the Rietveld method, for different thermal treatments (the average error found was ±0.0005 nm)

Phase		Thermal treatments at 1003 K					Thermal treatments at 1023 K			
		3.5 h	6.5 h	10.5 h	12 h	24 h	0.5 h	1.5 h	3.5 h	19.5 h
β-eucryptite	*a*	0.5190	0.5191	0.5190	0.5188	0.5182	0.5188	0.5181	0.5178	0.5183
s.s	*c*	0.5440	0.5450	0.5444	0.5444	0.5441	0.5438	0.5442	0.5448	0.5444
β-spodumene	*a*	n.d.[a]	n.d.[a]	n.d.[a]	n.d.[a]	0.7506	n.d.[a]	n.d.[a]	0.7516	0.7506
s.s.	*c*	n.d.[a]	n.d.[a]	n.d.[a]	n.d.[a]	0.9114	n.d.[a]	n.d.[a]	0.9123	0.9116

[a] Not detectable (below the sensitivity limit of the technique).

isothermal temperature was carried out, as already indicated, at 1003 and 1023 K, using a glass very rich in nuclei (i.e., the glass nucleated at 953 K for 20 h). Fig. 7 shows the crystallized mass percentage, determined using the Rietveld method, of the two solid solutions, which were formed one after the other, in strict correlation. The interpolated trends (continuous lines) in the plots were obtained by means of Avrami-like functions [19]. However, for the complexity of the crystallization processes it was not possible to apply Avrami's theory precisely, which theory was developed to explain the growth behavior of only one crystallizing phase. It is interesting to note, from this figure, that a decrease in β-eucryptite s.s is simultaneous with a corresponding increase in β-spodumene s.s. This is very probably due to the fact that β-eucryptite s.s. transforms itself continuously, with the increasing duration of the isothermal treatment, into the correlated structure of β-spodumene s.s (consecutive transformation). As a result, the glass-ceramic specimens, heated at 1003 K for 10 and 12 h, showed a good transparency (with a slight orange tint) having a fairly high crystallinity (about 77 and 78 wt%, respectively, as the sum of the two solid solutions formed in the sample, see Table 2).

4. Discussion

4.1. The nucleation stage

Since the size of the nucleated crystallites is very small, i.e., 4.0 ± 0.6 nm, which was determined by applying the Fourier line broadening method to the most intense 1 1 1 peak profile of $ZrTiO_4$, and such crystallites slightly increase with the subsequent thermal treatment, except for the most crystallized sample, for which the crystallite growth is much more evident, we can suppose that the nuclei are constituted by single domain parti-

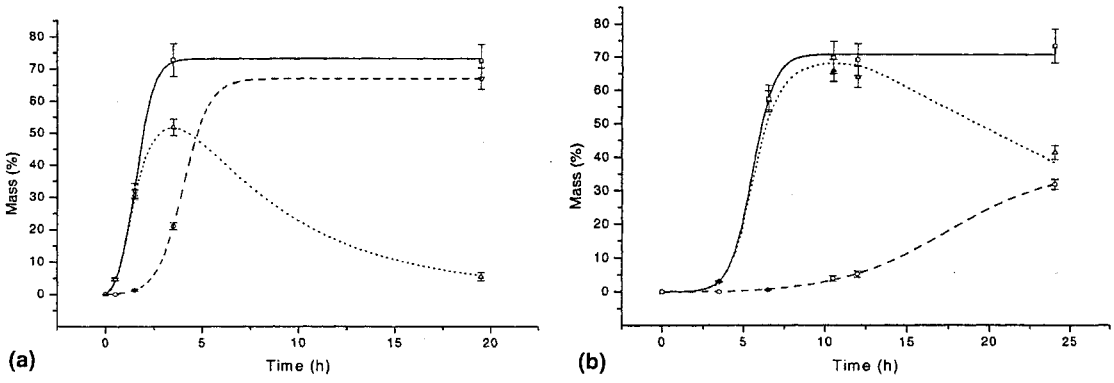

Fig. 7. The isothermal evolution of the crystallized mass, determined using the Rietveld method, of the two solid solutions at 1023 (a) and at 1003 K (b) is shown (β-eucryptite s.s.: triangles; β-spodumene s.s.: circles; sum of both phases: squares). The interpolated continuous lines were obtained by means of Avrami-like functions [24].

cles. This was also confirmed by TEM observations. With this hypothesis, it was possible to evaluate the average number of crystalline nuclei per volume unit of nucleated phase. Obviously, in order to evaluate such a number by using X-ray powder diffraction data only, it is necessary to know the composition of the nucleated phase, as in the present case.

The nuclei concentration is given by the following equation:

$$c_n(\text{nuclei/cm}^3) = \frac{m\rho_g}{V_n\rho_n}, \tag{6}$$

where m is the mass fraction of the nucleated phase, as determined by the Rietveld method; ρ_g is the glass density; ρ_n is the density of $ZrTiO_4$, as determined by the present X-ray data; V_n is the average nucleus volume, as obtained from the average $\langle D\rangle_{111}$ crystallite size for spherical particles. For a measured nucleus size of 4×10^{-7} cm, the above relation gives $c_n = 7.8 \times 10^{16}$(nuclei/ cm^3) for the $ZrTiO_4$ nuclei concentration.

Taking into account the appropriate magnification, the HRTEM micrographs reported in Fig. 4 give for both spheroidal crystals, there shown, a diameter of about 5 nm. This result is in good agreement with the average value of about 4 nm, determined by means of XRD line broadening. A number of 17–18 parallel planes can be observed inside these crystals, corresponding to a lattice spacing of about 0.28 nm. This spacing is close to the d_{111} interplanar distance of the $ZrTiO_4$ crystal structure (0.2927 nm). Fig. 8 shows the histogram of the relative frequency versus the nuclei size, determined by suitably observing and measuring about 300 particles in different TEM micrographs. From this plot a volume-weighted average size for the nuclei was calculated to be 2.9 ± 0.8 nm, in fairly good agreement with the XRD results. The nuclei concentration value c_n was also determined by counting about 300 nuclei in different TEM micrographs. Assuming an approximate thickness of 100 nm, a value of c_n of 9.6×10^{16} was obtained, close enough, for this type of approximate calculations, to the XRD value above reported.

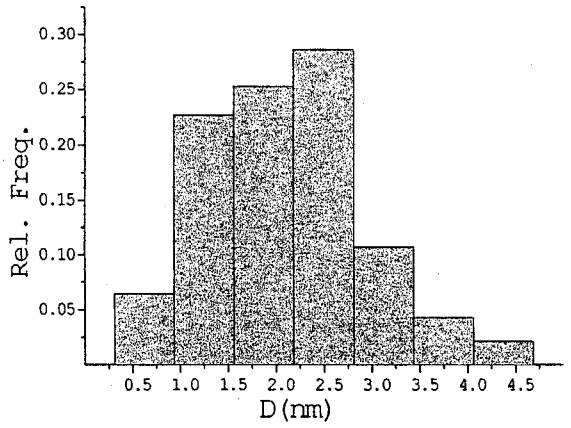

Fig. 8. Histogram of the relative frequency of the nuclei sizes, measured by observing a suitable number of TEM micrographs.

4.2. The crystallization stage

It is interesting to note that the average sizes of the crystalline nuclei of $ZrTiO_4$ were found to be 4.3, 4.0 and 4.8 nm for the samples crystallized at 1023 K for 0.5, 1.5 and 3.5 h, respectively. All these values are close to that of 4.0 nm found for the nucleated glass, while the size increased to 9.5 nm for the sample crystallized at 1023 K for 19.5 h (the error for all the reported nuclei sizes is ±15%). This behavior is probably due to the fact that, during the crystallization stage, each nucleus remained isolated inside the β-eucryptite crystal which grows all around it, except for the final very long thermal treatment of 19.5 h, which causes an uncontrollable growth process in the titanate crystals.

The unit cell parameters reported in Table 2 are very close (within ±0.0005 nm) to each other, for the β-eucryptite as well as for the β-spodumene phase, respectively, showing that, in all samples, very similar β-eucryptite solid solutions as well as very similar β-spodumene solid solutions were formed. In the case of the β-eucryptite s.s, the final unit cell parameters were refined and, on the basis of a published [20] study on the relationship between the chemical composition and unit cell parameters in the β-quartz/β-eucryptite system, we found, for β-eucryptite s.s, a composition of $Li_{1.13}Al_{1.13}Si_{2.87}O_8$, which is considerably richer in silica, with respect to the stoichiometric

β-eucryptite ($Li_2Al_2Si_2O_8$). This composition of the β-eucryptite s.s and the relevant occupation numbers fitted the XRD pattern well using the Rietveld refinement.

On the other hand, in the case of the β-spodumene s.s. phase, it was possible, in the sample crystallized at 1023 K for 19.5 h, to refine simultaneously the unit cell parameters, as well as the occupation numbers, thus obtaining a composition of $Li_{0.83}Al_{0.83}Si_{3.17}O_8$. This composition is close enough to $LiAlSi_3O_8$, which is reported in the literature. In fact, the lattice parameters found here are very close to those [$a = 0.75053(9)$ nm and $c = 0.9070(1)$ nm] found by other authors [21] when pertaining to this type of β-spodumene s.s., which is richer in silica, with respect to the stoichiometry of the β-spodumene ($Li_{1.33}Al_{1.33}Si_{2.67}O_8$), as also previously reported by Finlayson and Williams [22] and by Skinner and Evans [23].

It is interesting to note, from Fig. 7, that a decrease in β-eucryptite s.s is simultaneous with a corresponding increase in β-spodumene s.s. This is probably due to the fact that β-eucryptite s.s. transforms itself continuously, with the increasing duration of the isothermal treatment, into the correlated structure of β-spodumene s.s (consecutive transformation).

5. Conclusion

This research is part of a broader study aimed at assessing the possibilities of using glass-ceramics of the system Li_2O–Al_2O_3–SiO_2 (with small quantities of other oxides added for the nucleation stage or for other different technological purposes) for the production of transparent or translucent glazes with a shiny and bright surface and having high wear resistance properties. This preliminary investigation aims at improving knowledge of the mechanisms leading to the development of transparent/opaque materials during the thermal treatment of Li_2O–Al_2O_3–SiO_2 glass-ceramics. By employing DTA, XRD and TEM techniques, this study has succeeded in obtaining useful correlations between the nucleation and the crystallization processes, as well as in following the kinetics of crystal growth at two isothermal temperatures during the transformation of the first crystallized phase (β-eucryptite s.s.) into the second one (β-spodumene s.s.). This transformation was found to be a consecutive solid state reaction. The chemical composition of β-eucryptite s.s., as obtained by the Rietveld refinement, was found to be considerably richer in silica, with respect to the stoichiometric β-eucryptite, i.e., close enough to that of stoichiometric β-spodumene. Using the Rietveld refinement the composition of β-spodumene s.s. was found to be richer in silica too.

As a result, the glass-ceramic specimens, heated at 1003 K for 10 and 12 h, showed a good transparency (with a slight orange tint) having a fairly high crystallinity (about 77 and 78 wt%, respectively, as the sum of the two solid solutions formed in the sample, see Table 1).

References

[1] G.H. Beall, B.R. Karstetter, H.L. Rittler, J. Am. Ceram. Soc. 50 (1967) 181.
[2] G.H. Beall, D.A. Duke, J. Mater. Sci. 4 (1969) 340.
[3] P.W. McMillan, Glass-Ceramic, Academic, London, 1979.
[4] M. Grayson (Ed.), Encyclopedia of Glass, Ceramic, and Cement, Wiley, New York, 1985, p. 548.
[5] G. Partridge, S.V. Phillips, Glass Technol. 32 (1991) 82.
[6] G.H. Beall, L.R. Pinkey, J. Am. Ceram. Soc. 82 (1999) 5.
[7] P. Riello, P. Canton, G. Fagherazzi, J. Appl. Cryst. 31 (1998) 78.
[8] A. Sakthivel, R.A. Young, User's Guide to Programs DBWS-9006PC, Georgia Institute of Technology, Atlanta, GA, 1990.
[9] P. Riello, G. Fagherazzi, D. Clemente, P. Canton, J. Appl. Cryst. 28 (1995) 115.
[10] P. Riello, G. Fagherazzi, P. Canton, Acta Cryst. A 54 (1998) 219.
[11] W. Ruland, Acta Cryst. 14 (1961) 1180.
[12] S. Ottani, P. Riello, S. Polizzi, Powder Diffract. 8 (1993) 149.
[13] G. Fagherazzi, P. Canton, P. Riello, F. Pinna, N. Pernicone, Catal. Lett. 64 (2000) 119.
[14] S. Enzo, S. Polizzi, A. Benedetti, Z. Kristallogr. 170 (1985) 275.
[15] S. Enzo, G. Fagherazzi, A. Benedetti, S. Polizzi, J. Appl. Cryst. 21 (1985) 536.
[16] A. Marotta, A. Buri, F. Branda, J. Mater. Sci. 16 (1981) 341.
[17] T. Wakusugi, L. Burgner, M.C. Weinberg, J. Non-Cryst. Solids 244 (1999) 63.

[18] R.E. Newnham, J.Am. Ceram. Soc. 50 (1967) 216.
[19] J.W. Christian, in: The Theory of Transformation in Metals and Alloys, Part I, Pergamon, Oxford, 1975, p. 1.
[20] K. Nakagawa, T. Izumitani, J. Non-Cryst. Solids 7 (1972) 168.
[21] JCPDS-ICDD file No. 35/794, Nat. Bur. Stand. (U.S.), Monogr. 25, 21 76 (1984).
[22] F.M. Finlayson, J.P. Williams, J. Am. Ceram Soc. 50 (1967) 121.
[23] B.J. Skinner, H.J. Evans Jr., Am. J. Sci., Bradley 258 (1960) 312.
[24] Y. Takeuchi, Mineralog. J. (Japan) 2 (1958) 311.
[25] R.A. Young, The Rietveld Method, IUCR–Oxford University, Oxford, 1993, Chapter 1.

Nanostructure of Pd/SiO_2 supported catalysts

Stefano Polizzi,*[a] Pietro Riello,[a] Antonella Balerna[b] and Alvise Benedetti[a]

[a] *Dipartimento di Chimica Fisica, Università Ca' Foscari di Venezia, Via Torino 155/b, I-30170 Mestre-Venezia, Italy. E-mail: polizzi@unive.it*

[b] *INFN-Laboratori Nazionali di Frascati, Via E. Fermi 40, I-00044 Frascati (RM), Italy*

Received 26th June 2001, Accepted 21st August 2001
First published as an Advance Article on the web 27th September 2001

Pd/SiO_2 supported catalysts were investigated using anomalous small-angle X-ray scattering (ASAXS), wide-angle X-ray scattering (WAXS), transmission electron microscopy (TEM) and extended X-ray absorption fine structure spectroscopy (EXAFS). Samples containing about 3 wt.% and 6 wt.% of metal were obtained by impregnation, calcined at 773 K and reduced at 623 K. Two populations of nanoparticles were found in both samples. In the 3 wt.% sample, one population consisted of very small nanoparticles (average 3 nm), and the other of larger ones (average 13 nm). A higher metal load seems to cause a broadening of the size distribution of the first population and a consequent increase in its average dimension (6 nm), rather than to influence the larger nanoparticles. Despite the relatively high metal content and temperatures, the population of small particles was predominant in both samples: 80% in the 3 wt.% sample and 57% in the 6 wt.% one. A large number of the smallest particles (< 3 nm) was present in the 6 wt.% sample as well, and the total metal surface available was about the same in the two samples in spite of the different amounts of metal. Anomalous scattering has proven to be essential to quantitative analysis.

Introduction

Metal supported catalysts are composed of catalytically active metal particles dispersed in an inert porous matrix. Since catalysis takes place at the surface of the metal particles, the most efficient use of the expensive metal can be achieved with very small particles, for which the surface/volume ratio is maximized. Furthermore, below a certain dimension, changes in the electronic structure take place that may further enhance the specific catalytic efficiency (selectivity and/or activity) of some metals. This critical dimension is metal specific, but is usually in the 1–3 nm range.[1]

For these reasons, chemical engineers strive to produce particles that are well dispersed and as small as possible. Yet, for the most common techniques of characterization, 1–3 nm is a critical dimension, especially when the system also contains larger nanoparticles (10–20 nm). For example, chemisorption gives only an average size, whereas wide-angle X-ray scattering (WAXS) peaks for 1–3 nm particles become so broad that they vanish in the amorphous halo of the support or in the tails of peaks due to larger particles, if present. Moreover, samples of industrial importance usually contain low metal fractions, which means low signal levels for X-ray studies. Also, observation by transmission electron microscopy (TEM) becomes difficult when such small particles are encapsulated in a porous matrix.

In contrast, extended X-ray absorption fine structure spectroscopy (EXAFS) and anomalous small-angle X-ray scattering (ASAXS) are able to detect such small particles,[2–5] and in particular ASAXS can also provide quantitative information when larger nanoparticles are simultaneously present. In some cases, Rietveld analysis of WAXS data can give an indirect support to these findings.[6–8]

In all the charcoal supported catalysts loaded with Au or Pd or both, and prepared by impregnation, which our group have studied, we have shown[3,4] that a population of small nanoparticles measuring 1–3 nm is usually obtained together with a population of larger nanoparticles with a mean size of 10–20 nm. We think that this finding must be considered characteristic of the particular method of preparation used, even though the generality of these results must still be verified. One of the basic problems is the understanding of the role of the different parameters that control the ratio between these two populations of metal particles, such as metal load or calcination and reduction temperature.

In our earlier studies[3–8] we dealt with samples of industrial importance that usually contain low metal fractions (lower than 1 wt.%) and are reduced at low temperatures (T < 350–370 K). For these kinds of samples, a high percentage of small particles can be expected, given the very high dilution of the metal phase and the moderate reduction treatment. Under these conditions, the sintering of the crystallization nuclei of the parent salt is likely to be hindered by a lower diffusion coefficient on the surface of the support.

In the present paper we deal with samples loaded with a higher metal content and heat-treated at higher temperatures. We report a detailed ASAXS study of two "model" Pd/SiO_2 catalysts loaded with a metal percentage of about 3 wt.% (sample A) and 6 wt.% (sample B), calcined at 773 K and reduced at 623 K. The aim of the work is to show that: (i) by using impregnation synthesis, very small particles are present also in the aforementioned conditions where sintering is more likely to occur; and (ii) ASAXS is able to give quantitative information on sizes and the relative amounts of different particle populations, also when highly energetic X-rays are needed (Pd K absorption edge). The study is also supported by TEM, EXAFS and WAXS measurements.

Experimental

Catalysts were prepared by impregnation of SiO_2 (Akzo Chemie F22; surface area 400 $m^2\ g^{-1}$, particle size range 100–150 μm) with aqueous solutions of H_2PdCl_4. After drying at 383 K for 18 h, samples were calcined at 773 K for 1 h, then

 DOI: 10.1039/b105607g

reduced at 623 K for 2 h and passivated (5% O_2 in Ar) before storing exposed to normal room conditions. The Pd content was 2.9 wt.% (sample A) and 5.6 wt.% (sample B), as determined by atomic mass spectroscopy (Perkin Elmer model 500).

ASAXS measurements were taken at the JUSIFA small-angle scattering beamline[9] of the DORIS synchrotron radiation source in DESY (Hamburg). Measurements were performed under vacuum in transmission geometry at different energies near the Pd K absorption edge (E_0 = 24 350 eV). Data were recorded with a two-dimensional position-sensitive gas-filled multi-wire proportional counter. Data were fitted by two Schulz distributions of spherical particles. Experimental details, data evaluation and a discussion of the measuring strategy are reported elsewhere.[5]

WAXS data were collected with a Philips X'Pert diffractometer with Ni-filtered CuKα radiation, a graphite monochromator on the diffracted beam, and a proportional counter with electronic pulse height discrimination. An angular step of 0.05° and a collection time of 10 s per point in several runs were used. Line broadening analysis was carried out using a previously published method[10] that employs the analytical Fourier transform of the fitted function. Volume weighted distributions of sizes are calculated for spheres. For the Rietveld analysis, a modified program[11,12] was used, which is able to separate the contribution of different phases and quantitatively determine their relative amounts by using the integrated scattered intensity of each phase. In the fitting procedure the theoretical intensity is written as:

$$Y - Y_{air} = K_{Pd}\, Y_{Pd} + K_{Si}\, Y_{Si}$$

where $Y - Y_{air}$ is the air-corrected diffraction pattern, Y_{Pd} is the contribution of the crystalline metal, Y_{Si} that of the silica support and K_{Pd} and K_{Si} are refinable scale factors.

TEM images were taken with a Jeol 3010, operating at 300 kV, equipped with a Gatan (Warrendale, PA, USA) multi-scan CCD camera (model 794) and an Oxford Instrument (Oxford, UK) EDS microanalysis detector (model 6636). The sample was dispersed in an isopropyl alcohol solution and deposited on a carbon holey film.

EXAFS measurements were performed at the European Synchrotron Radiation Facility (ESRF) on the Italian beamline GILDA.[13,14] Specimens were prepared by mixing the fine powder of the samples with boron nitride, and pressing the mixture into pellets. The Pd amount was chosen in order to achieve an edge jump of approximately 0.9. The spectra of the reference sample (Pd foil) and of the silica supported samples were recorded under vacuum in transmission mode (for comparison with ASAXS, no special atmosphere was used). All spectra were recorded at 77 K to reduce thermal effects. Data were analyzed using the GNXAS package,[15,16] which allows one to decompose the EXAFS signal in terms of irreducible n-body contributions $\gamma^{(n)}$. The theoretical signal is calculated as a sum of the relevant $\gamma^{(n)}$ functions, also taking into account multiple scattering processes, and fitted to the experimental one by refining the interatomic distances, the angles of the n-atom bodies, the coordination numbers and the Debye–Waller factors. Errors in the parameters are evaluated according to the size of the ellipse in parameter space enclosing χ^2 values with a confidence of 95%.

Results and discussion

In Fig. 1, reflections of the Pd fcc phase can be seen on the silica amorphous halo in the WAXS spectra of both samples. However, it can be noted that the peaks relevant to sample A are much lower than one would expect on the basis of the metal fraction. In fact, the area of the 111 peak of sample A is about a quarter of that of sample B, whereas the metal load is about a half. This is an indication of the presence in sample A

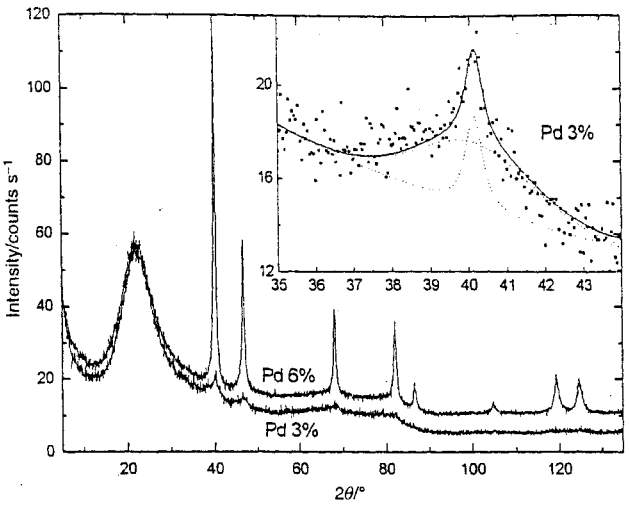

Fig. 1 Wide-angle X-ray scattering (WAXS) data of the two analyzed Pd/SiO_2 catalysts. Inset: fitting of the Pd 111 reflection of sample A by two pseudo-Voigt functions.

of a large number of particles smaller than about 3 nm, since the contribution of such particles tends to disappear from the diffraction peaks and merge with the amorphous halo. In the inset of Fig. 1, the Pd 111 peak of sample A is enlarged. The reflection profile has a peculiar, super-Lorentzian shape, which is typical of a bimodal crystallite size distribution.[17] In fact, this reflection can also be fitted very well by two pseudo-Voigt functions with different widths but centered at the same angular position (see inset of Fig. 1), representing the contributions of nanoparticles with average diameter of 3 nm (broader peak) and larger nanoparticles of about 16 nm (narrower main peak) (average values obtained from the volume weighted distributions of spheres in Fig. 2). By dividing the area of the narrower peak by the sum of the areas of the two peaks, the larger particles should be 43% of the total volume. Yet, as noted above, the peak area of sample A seems to be underestimated. Instead, if one divided by half of the peak area of sample B, one would find that only 19% of the metal volume consists of such larger particles. Apparently, also when attempting to describe the presence of small particles by using a separate peak, the contribution of the smallest particles (probably smaller than 2 nm) tends to be underestimated, as the ASAXS measurements confirm (see below). A portion of these nanoparticles might also be oxidized as will be shown by the EXAFS measurements, thus scattering in a position slightly shifted from the main peaks of pure palladium. In both cases, the intensity could be so small that the scattering is definitely lost in the background. Unfor-

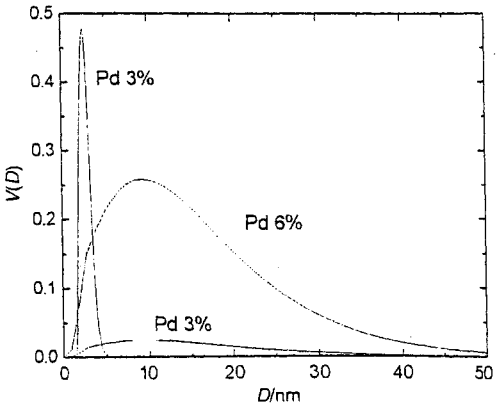

Fig. 2 Volume weighted particle (spheres) size distributions of samples A (two populations) and B obtained by line profile analysis of WAXS data. The area below the curves is proportional to the metal volume.

tunately, these rough findings could not be substantiated with a more precise quantitative analysis using the Rietveld method, because the peaks measured for sample A are too weak.

On the other hand, the line shape of sample B has only a small super-Lorentzian character, and can be fitted fairly satisfactorily by using a single peak. Line broadening analysis gives an average size of 16 nm, but the distribution (see Fig. 2) actually reaches its maximum at about 9 nm and is very much skewed at higher values (if a super-Lorentzian is used, a shoulder of a second population is also present). In this case, it was possible to carry out a quantitative Rietveld analysis. The analyzed crystalline peaks account for a 5.2 wt.% metal content, which confirms with a reasonable uncertainty of 5% that the crystalline peaks seem to account for all the metal. So, Rietveld analysis indicates that, if a fraction of nanoparticles is present in sample B, within a 5% error this corresponds to a fraction smaller than 0.3 wt.% of metal. In Table 1, the average sizes obtained by the different techniques are compared. It should be noted that the presence of a portion of partially oxidized particles can partly invalidate the quantitative Rietveld analysis. For this reason, in one recent paper,[8] we performed the measurements under a controlled atmosphere, in order to transform all the metal into the metallic state. In the present case, this did not seem necessary since EXAFS measurements (see below) have shown that, within the sensitivity of the technique, no oxidized particles are present in sample B. However, we would like to emphasize that the comparison between the metal amount determined by atomic mass spectroscopy and the quantitative determination of the metal investigated by a certain technique is very important. Only in this way is one able to understand if the technique used is giving a representative image of the sample, or if the microstructural information relates to only a part of the sample. ASAXS seems to be less sensitive to this problem than Rietveld analysis, even if ASAXS quantitative analysis requires a very careful control of all the experimental parameters. It must also be noted that for Pd/SiO_2 samples the present detection limit has been found[5] to be around 2 wt.% of Pd content, whereas metal fractions as low as 0.2 wt.% could be detected in other catalysts.[4,6] In the present case, the metal content determined by ASAXS was 2.7 ± 0.4 wt.% and 5.3 ± 0.8 wt.% for samples A and B respectively (the large relative uncertainties are mainly due to different possible choices of the electronic difference to be used in the calculation, rather than to experimental errors[5]). Thus, we can be fairly confident that the nanostructural analysis we carried out by ASAXS affects all the palladium phase loaded in the catalysts.

The ASAXS data shown in Fig. 3 clearly indicate the presence of bimodal distributions of particle sizes in both samples, as shown in Fig. 4. This technique allowed us not only to confirm the volume weighted average size of 3 nm obtained by WAXS for the distribution of small particles for sample A, but also to show that a population of bimodal distribution is in fact also present in sample B. The distribution of smaller particles becomes broader and its average size consequently shifts to 6 nm. Furthermore, the quantitative data analysis shows that, for sample A, the population of small particles makes up

Table 1 Average particle sizes[a]

Sample	WAXS[b] (LB)		ASAXS[b]		EXAFS	
A (3 wt.%)	3	16	3	13	1.5	—
B (6 wt.%)	16		6	15	5[c]	—

[a] About 10% error estimated. [b] Volume weighted value. [c] About 20% error estimated.

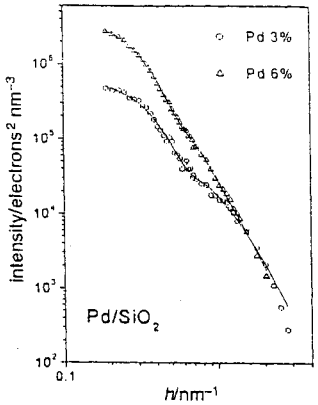

Fig. 3 Anomalous small-angle scattering (ASAXS) data of samples A (○) and B (△), obtained by subtracting normalized curves at energy E_1 from those at E_5, and best-fitted distribution functions (solid lines).

80% of the total mass of the metal, and that also for sample B small nanoparticles represent 56% of the metal. In terms of number of particles, this means that the small particles are also an overwhelming majority in sample B. In fact, the two scattering curves in Fig. 3 overlap in the high h range, which indicates that the total metal surface is almost the same in the two samples in spite of the different metal loads: in the 3 wt.% sample, the metal is used much more efficiently because of the large amount of very small particles. The shape of the distribution for sample B (see Fig. 4) shows that a fraction of very small nanoparticles is also present in this material, which probably accounts for the small super-Lorentzian character of the WAXS peaks and the slightly lower value of metal content found when using the Rietveld method instead of mass absorption technique. The presence of such small particles has been confirmed by TEM (see below). The remaining part of the metal is made up of larger nanoparticles with average sizes of 13 nm for sample A and 15 nm for sample B in agreement with the WAXS results (see Table 1).

In Table 1 the average sizes of the particles in samples A and B are compared. It can be seen that the average size of the population of small particles increases as the metal load is increased, whereas that of the population of larger nanoparticles remains almost constant. A previously investigated[4] sample of Pd/C containing only 0.7 wt.% of metal and prepared at a lower temperature fits nicely into this trend, having two populations with average sizes of 1 nm and 14 nm. Since the heat treatment procedure undergone by samples A and B was the same, it can be argued that the effect is mainly due to the metal load and not to the heat treatment. It may be noticed that, as the metal load increases, more and more of the population of small particles will contribute to the main

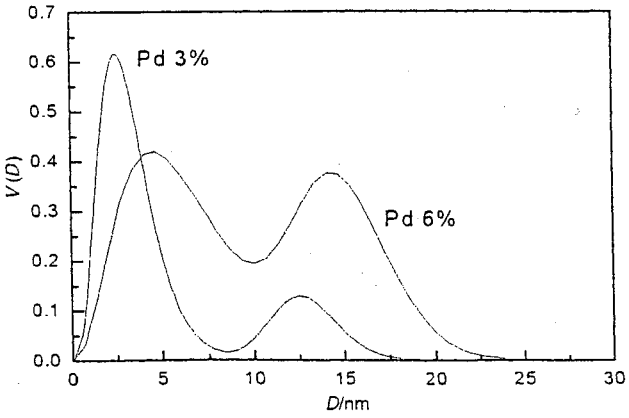

Fig. 4 Volume weighted particle (spheres) size distributions obtained from ASAXS data. The area below the curves is proportional to the metal volume.

WAXS peak and will be assigned by Rietveld analysis to the population of nanoparticles. In contrast, ASAXS is still able to separate the two populations neatly. In conclusion, ASAXS data clearly show that despite the high metal load and temperatures the impregnation method is able to yield a large number of very fine metal particles.

The EXAFS spectra confirmed the presence of the population of small particles and further evidenced that, while metal particles in sample B are in the metallic state, in sample A a fraction of the particles is oxidized. Fig. 5 shows the X-ray absorption near-edge structure (XANES) spectra of the Pd foil and of the two silica supported samples. Whereas the absorption edge of sample B is very similar to that of the palladium foil, that of sample A shows some differences in the near-edge region, which indicate, as will be shown by the EXAFS data analysis, that about 30% of the palladium atoms present in the sample are in an oxidized sate.

Fig. 6 shows the k^2 weighted Fourier transforms of the experimental and theoretical EXAFS or $\chi(k)$ signals of the two samples, together with that of the reference sample; in Table 2

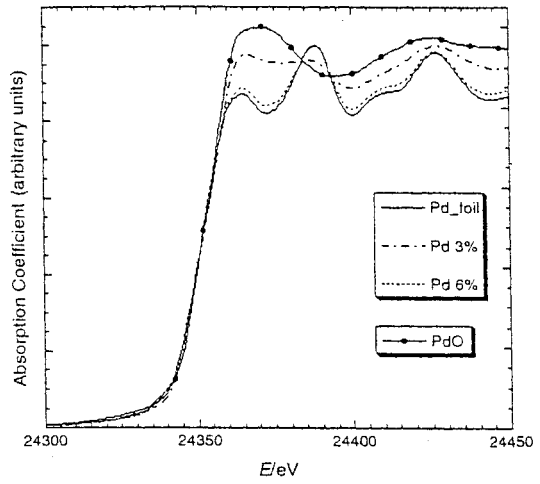

Fig. 5 XANES spectra of the two samples and of the Pd reference foil. The XANES spectrum of PdO is also included for comparison.

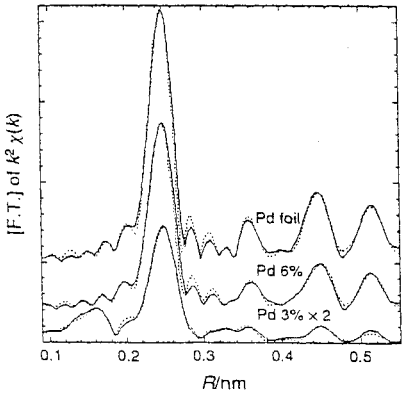

Fig. 6 Fourier transforms of the experimental and theoretical EXAFS signals.

the best-fit parameters are reported. In sample B, the interatomic distances (R) found are in agreement with those of the reference metallic foil. The coordination numbers (N) and Debye–Waller factors (σ^2) are different from the bulk ones, showing the presence of small metal particles. The reduction of the coordination numbers was used to estimate[16] the average particle size of sample B under the hypothesis of a spherical shape, and the value found (5 nm) agrees with WAXS and ASAXS results, within the method's estimated 20% uncertainty.

The analysis of sample A was more complicated since Pd is present in two different phases, one metallic and the other oxide. For the metallic phase, the interatomic distances found are comparable with the ones of the metallic foil. For the oxide phase, the distances found are comparable with the ones of palladium oxide having a simple tetragonal structure[18] with a Pd–O contribution at 0.201 nm and two Pd–Pd contributions at 0.304 nm and 0.339 nm. Due to the presence of the two phases, it was not possible to use the same procedure used for sample B when evaluating the mean dimension of the Pd particles. In fact, the N values found are not the real coordination numbers, but are weighted by the atomic percentage of Pd atoms present in each phase. Using the procedure reported in ref. 19, a rough estimation of the average size could be achieved and the atomic percentage of Pd atoms in the metallic phase could be estimated. It was found that, in sample A, the metal nanoparticles have a mean dimension of about 1.5–2 nm and that about 70% of the Pd atoms are in the metal phase. This agrees with the ASAXS and WAXS results.

It is clearly evident that, for both samples, the particle dimension given by the EXAFS data analysis corresponds only with one of the two components found by ASAXS and WAXS. In the presence of a distribution of different particle sizes, EXAFS gives a mean dimension weighted by the fraction of atoms corresponding to the different sizes. In both samples, as shown by ASAXS and partially by WAXS, the largest amount of Pd atoms is in the smaller particles. This explains why the larger ones are not revealed by EXAFS.

The electron microscope visually supports the findings of the other techniques. Fig. 7(a) shows a typical low magnification TEM image of a Pd/SiO_2 sample. One large silica agglomerate reaches out into a hole of the carbon film, and palladium particles are visible as darker dots on the granular structure of the silica. The metal particles are visible due to their higher absorption and, in some cases, to diffraction effects as well. Agglomeration of the metal particles occurs, but the overall dispersion is good. As the magnification increases [see Figs. 7(b) and (c)], more and more smaller particles become visible as well defined round-shaped zones or as darker areas with blurred contours. In Figs. 8(a) and (b), similar areas of the two samples are compared. In sample A, metal particles look smaller and better dispersed than in sample B. Nanoparticles as small as about 1 nm seem to be present in sample A, while in sample B the smallest particles that we were able to detect were larger than 2 nm [see Fig. 8(b)]. Furthermore, the occurrence of these particles seems to be lower in sample B. Fig. 9 shows three high resolution images of some of the smallest particles found in sample B. No

Table 2 EXAFS fitting results: interatomic distances (R), coordination numbers (N) and Debye–Waller factors (σ^2) of the first, second and third coordination shells

Sample		R_1/nm	N_1	$\sigma_1^2 \times 10^{-5}$/nm^2	R_2/nm	N_2	$\sigma_2^2 \times 10^{-5}$/nm^2	R_3/nm	N_3	$\sigma_3^2 \times 10^{-5}$/nm^2
Pd foil	metal	0.275(1)	12	1.6(2)	0.388(2)	6	3.4(3)	0.478(3)	24	3.9(5)
A (3 wt.%)	metal	0.275(2)	5.1(5)	4.0(5)	0.387(3)	2.2(6)	7.5(5)	0.478(5)	8.4(7)	8.3(6)
	oxide	0.201(2)	1.8(7)	2.0(6)	0.304(3)	2.4(6)	13.0(6)			
					0.339(4)	3.4(6)	14.5(6)			
B (6 wt.%)	metal	0.275(1)	10.7(5)	2.0(2)	0.388(2)	5.3(3)	4.1(4)	0.477(5)	20(6)	6.2(5)

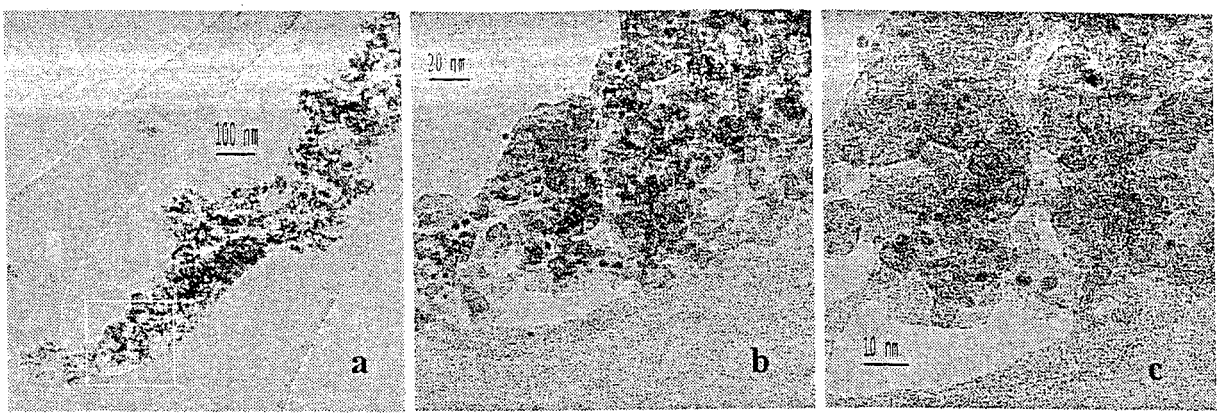

Fig. 7 Transmission electron images (TEM) of the same part of sample A at different magnifications. The white frame in (a) shows the area magnified in (b) and (c).

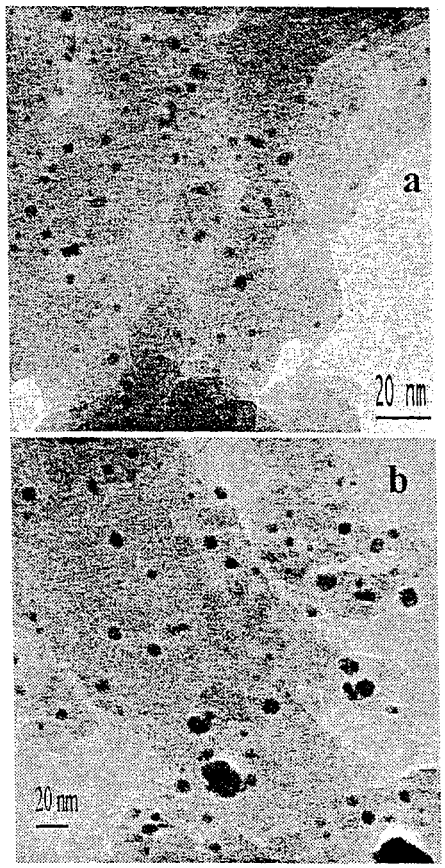

Fig. 8 Comparison of TEM images of similar area of sample A (a) and sample B (b).

particles smaller than about 2 nm showing a diffraction contrast have been found.

Conclusions

The aim of this paper was to investigate the simultaneous presence of one population of nanoparticles measuring 1–3 nm and one of larger particles in the 10–20 nm size range in two "model" Pd/SiO_2 catalysts prepared by impregnation and loaded respectively with 3 wt.% and 6 wt.% of metal. ASAXS and EXAFS data clearly show that, despite the high metal load and temperatures, the impregnation method is able to yield a component of very fine metal particles as previously found for other more diluted systems. ASAXS has shown that the amount of metal loading mostly influences the average size of the smaller nanoparticles, leaving the size of the larger ones almost unchanged. The average size of the small nanoparticles was approximately 3 nm for the sample loaded with less metal and approximately 6 nm for the other. Results were also supported by WAXS, EXAFS and TEM measurements.

Acknowledgements

This project was supported by the TMR-Contract ERBFMGECT950059 of the European Community. Financial support from MURST is also acknowledged. Prof. F. Pinna is greatly acknowledged for helpful discussions, and T. Fantinel and T. Finotto for experimental assistance in sample preparation and atomic mass spectroscopy measurements. ASAXS measurements could not have been carried out without the competent technical assistance of G. Goerigk and his advice concerning data collection and analysis.

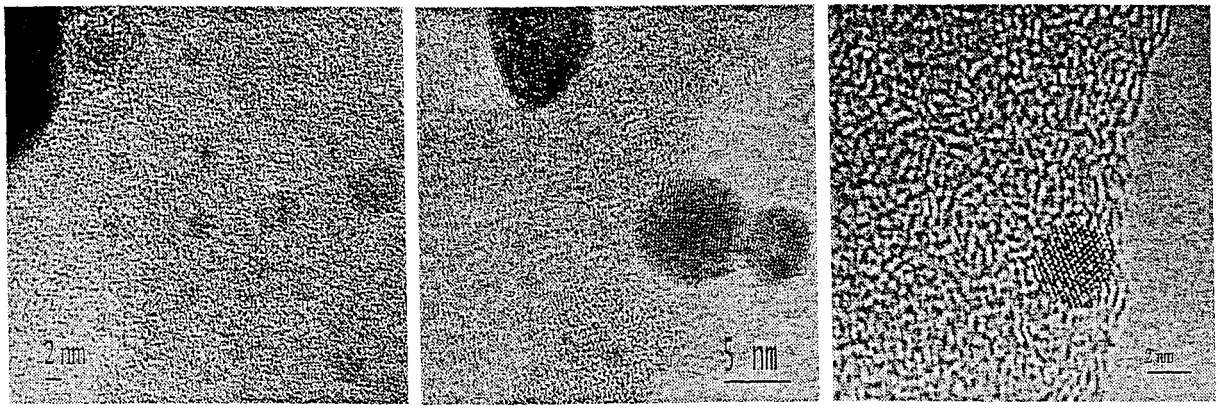

Fig. 9 Three high resolution TEM images of sample B.

References

1 A. Borodziski and M. Bonarowska, *Langmuir*, 1997, **13**, 5613.
2 A. Balerna, L. Liotta, A. Longo, A. Martorana, C. Meneghini, S. Mobilio and G. Pipitone, *Eur. Phys. J. D*, 1999, **7**, 89.
3 A. Benedetti, S. Polizzi, P. Riello, F. Pinna and G. Goerigk, *J. Catal.*, 1997, **171**, 345.
4 A. Benedetti, L. Bertoldo, P. Canton, F. Pinna, G. Goerigk, P. Riello and S. Polizzi, *Catal. Today*, 1999, **49**(4), 485.
5 S. Polizzi, A. Benedetti and P. Riello, *J. Appl. Crystallogr.*, to be submitted.
6 P. Riello, P. Canton and A. Benedetti, *Langmuir*, 1998, **14**, 6617.
7 P. Riello, P. Canton, A. Minesso, F. Pinna and A. Benedetti, *Stud. Surf. Sci. Catal. A*, 2000, **130**, 3273.
8 P. Canton, P. Riello, A. Furlan, A. Minesso, L. Bertoldo, F. Pinna and A. Benedetti, *Catal. Lett.*, 2000, **69**, 17.
9 H.-G. Haubold, K. Gruenhagen, M. Wagener, H. Jungbluth, H. Heer, A. Pfeil, H. Rongen, G. Brandenburg, R. Moeller, J. Matzerath, P. Hiller and H. Halling, *Rev. Sci. Instrum.*, 1989, **60**, 1943.
10 S. Enzo, S. Polizzi and A. Benedetti, *Z. Kristallogr.*, 1985, **170**, 275.
11 P. Riello, P. Canton and G. Fagherazzi, *J. Appl. Crystallogr.*, 1998, **31**, 78.
12 P. Riello, G. Fagherazzi and P. Canton, *Acta Crystallogr. A*, 1998, **54**, 219.
13 S. Pascarelli, F. D'Acapito, G. Antonioli, A. Balerna, F. Boscherini, R. Cimino, G. Dalba, P. Fornasini, G. Licheri, C. Meneghini, F. Rocca and S. Mobilio, *ESRF Newslett.*, 1995, **23**, 17.
14 S. Pascarelli, F. Boscherini, F. D'Acapito, J. Hrdy, C. Meneghini and S. Mobilio, *J. Synchrotron Radiat.*, 1996, **3**, 147.
15 A. Benedetti, G. Fagherazzi, S. Enzo and M. Battagliarin, *J. Appl. Crystallogr.*, 1988, **21**, 543.
16 A. Filipponi, A. Di Cicco and C. R. Natoli, *Phys. Rev. B*, 1995, **52**, 15122.
17 A. Filipponi and A. Di Cicco, *Phys. Rev. B*, 1995, **52**, 15135.
18 M. Borowski, *J. Phys. IV*, 1997, **7**, C2-259.
19 J. Waser, A. Levy and S. W. Peterson, *Acta Crystallogr.*, 1953, **6**, 661.